SANDIA REPORT

SAND2015-10453
Unlimited Release
Printed December 2015

Non-thermal x-ray emission from wire array z-pinches

David J Ampleford, Stephanie B Hansen, Christopher A Jennings, Timothy J. Webb, Victor Harper-Slaboszewicz, Guillaume P. Loisel, Timothy M. Flanagan, Kate S. Bell, Brent Jones, Leroy A. McPherson, Gregory A. Rochau, Jeremy P. Chittenden, Mark Sherlock, Brian Appelbe, John Giuliani, Nicholas Ouart, John Seely

Prepared by
Sandia National Laboratories
Albuquerque, New Mexico 87185 and Livermore, California 94550

Sandia National Laboratories is a multi-program laboratory managed and operated by Sandia Corporation, a wholly owned subsidiary of Lockheed Martin Corporation, for the U.S. Department of Energy's National Nuclear Security Administration under contract DE-AC04-94AL85000.

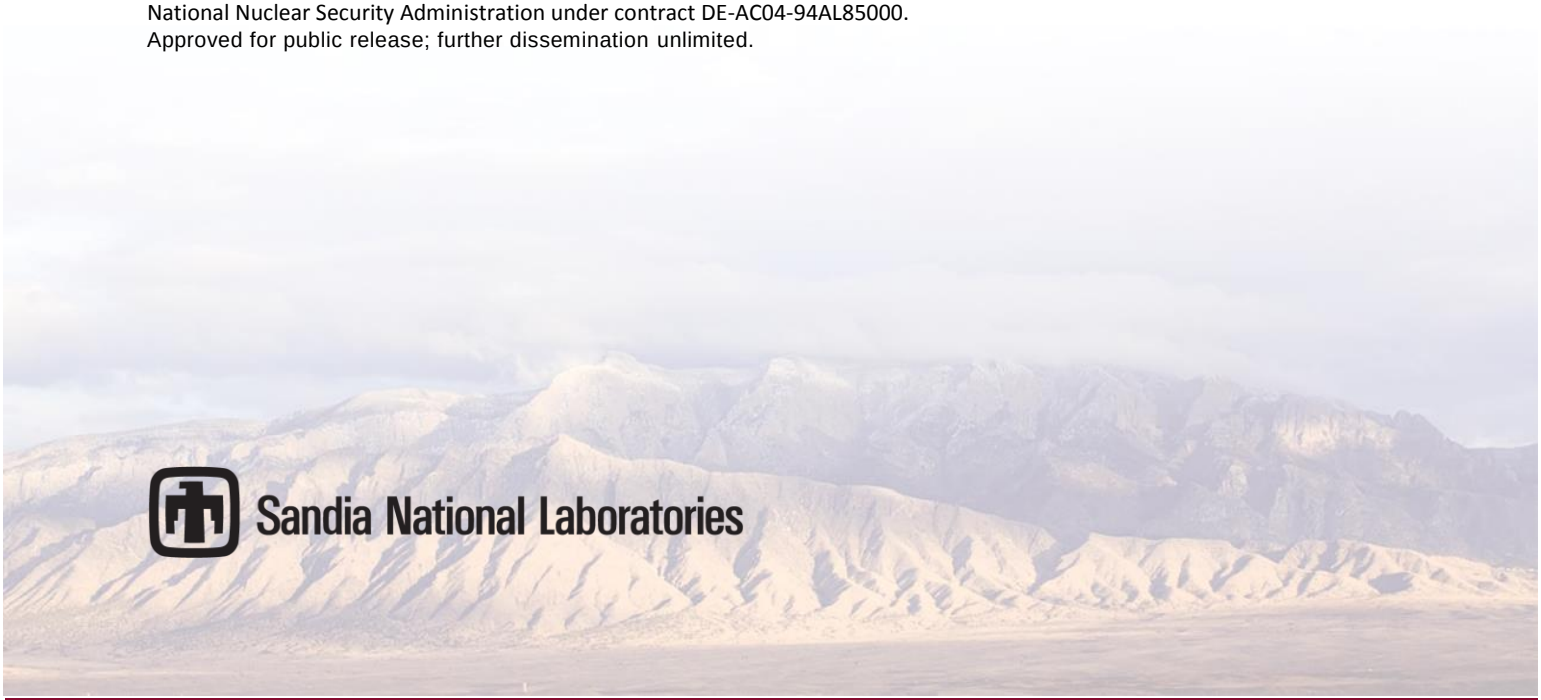

Sandia National Laboratories

Issued by Sandia National Laboratories, operated for the United States Department of Energy by Sandia Corporation.

Available to DOE and DOE contractors from
U.S. Department of Energy
Office of Scientific and Technical Information
P.O. Box 62
Oak Ridge, TN 37831

Telephone: (865) 576-8401
Facsimile: (865) 576-5728
E-Mail: reports@osti.gov
Online ordering: http://www.osti.gov/scitech

Available to the public from
U.S. Department of Commerce
National Technical Information Service
5301 Shawnee Rd
Alexandria, VA 22312

Telephone: (800) 553-6847
Facsimile: (703) 605-6900
E-Mail: orders@ntis.gov
Online order: http://www.ntis.gov/search

SAND2015-10453
Unlimited Release
Printed December 2015

Non-thermal x-ray emission from wire array z-pinches

David J Ampleford[1], Stephanie B Hansen[2], Christopher A Jennings[2], Timothy J. Webb[3], Victor Harper-Slaboszewicz[4], Guillaume P. Loisel[1], Timothy M. Flanagan[5], Kate S. Bell[5], Brent Jones[6], Leroy A. McPherson[7], Gregory A. Rochau[1]

1. Radiation & Fusion Experiments
2. Radiation & ICF Target Design
3. Advanced Radiographic Technologies
4. Radiation Effects Research
5. Radiation Effects Experimentation
6. Neutron & Particle Diagnostics
7. Imaging and Spectroscopy

Sandia National Laboratories, P.O. Box 5800
Albuquerque, New Mexico 87185-1106

Jeremy P. Chittenden, Mark Sherlock, Brian Appelbe
Blackett Laboratory, Imperial College London
London SW7 2AZ, United Kingdom

John Giuliani, Nicholas Ouart
Naval Research Laboratory
4555 Overlook Avenue SW
Washington, DC 20375-5346

John Seely
Artep Inc.
2922 Excelsior Springs Court
Ellicott City, Maryland 21042

Abstract

We report on experiments demonstrating the transition from thermally-dominated K-shell line emission to non-thermal, hot-electron-driven inner-shell emission for z pinch plasmas on the Z machine. While x-ray yields from thermal K-shell emission decrease rapidly with increasing atomic number Z, we find that non-thermal emission persists with favorable Z scaling, dominating over thermal emission for Z=42 and higher ($h\nu \geq 17$keV). Initial experiments with Mo (Z=42) and Ag (Z=47) have produced kJ-level emission in the 17-keV and 22-keV Kα lines respectively. We will discuss the electron beam properties that could excite these non-thermal lines. We also report on experiments that have attempted to control non-thermal K-shell line emission by modifying the wire array or load hardware setup.

ACKNOWLEDGMENTS

The authors thank many colleagues for useful discussions, including Dan Sinars, Mike Cuneo, Roger Vesey and Peggy Christensen. The authors are particularly grateful to the many teams who make experiments on Z possible, including Z load hardware, Z diagnostics, Lab 101, Z Center Section and many others.

The CRITR-X upgrade was designed and fabricated by the Artep Inc., Elicott City, MD, specifically by J. Seely, Uri Feldman, Layne Marlin. Calibration work was performed by ARTEP, at the National Institute of Standards and Technology (NIST), Gaithersburg, MD, with the help of C. Szabo-Foster, L. Hudson, S. Seltzer and M. O'Brien and in collaboration with G. Loisel at Sandia. The calibration analysis, the instrument modeling and further testing was conducted at Sandia. The authors would like to thank C. Ball, C. Bourdon, C. Coverdale, P. Lake, L. McPherson, G. Rochau for contributing for their support and useful discussions related to CRITR-X.

The results reported in Section 6 were obtained using the UK National Supercomputing Service ARCHER and the Imperial College supercomputer CX1.

This work was funded by Sandia LDRD project 117862. The authors thank the REHEDS LDRD panel for funding this work and for their continued support.

CONTENTS

FIGURES

TABLES

1 INTRODUCTION

1.1 Thermal and non-thermal K-shell emission

Wire array z-pinches on the Z generator have produced some of the most energetic and powerful x-ray sources in the 1-10 keV spectral range[1,2], as well as in the sub-keV spectral range[3,4]. For the 1-10 keV range, low Z materials from Al to Cu are used to create line radiation from highly charged ions. In this case the radiation is produced from ions in the K-shell producing Heα and Lyα emission (which we term here *thermal K-shell emission*; Figure 1a). There is an interest in developing higher photon energy sources on Z, however due to the increase in energy required to ionize to the K-shell as the atomic number is increased (hence increasing radiative losses), these thermal sources drastically drop in efficiency.

In this report we discuss evaluating Kα emission in wire array z-pinches as a >15 keV x-ray source. This emission from inner-shell ionization of ions that are not ionized to the K-shell (e.g. due to energetic electrons or photons interacting with the ion; Figure 1b) requires less energy to ionize and suffers smaller radiation losses, and hence should scale more favorably than thermal K-shell emission. As this emission is largely driven by non-thermal processes, we term it here *non-thermal K-shell emission*.

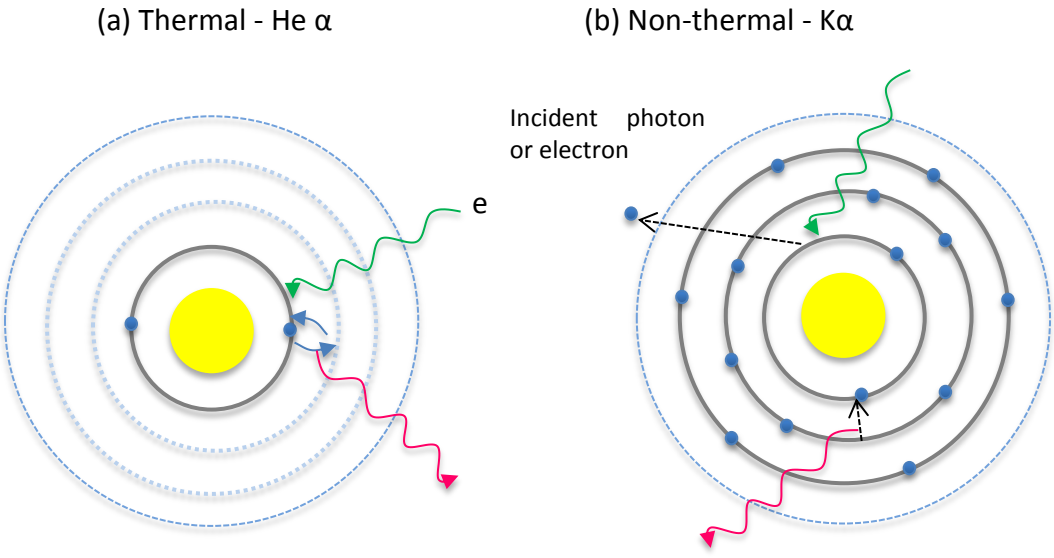

Figure 1: Physical difference between thermal Heα emission and non-thermal Kα emission

1.2 Scaling thermal and non-thermal emission to higher photon energies

For pulsed power experiments, the high internal energy required to radiate efficiently from the thermal K-shell is achieved by thermalizing the kinetic energy from a high velocity implosion. Reaching internal energies necessary for efficient K-shell radiation from high-Z materials thus requires high implosion velocities [1]

$$v_{imp} \sim ((2{:}024\eta Z^{3.662})/A)^{1/2}$$

where A is the atomic mass. The parameter η is a factor to account for radiative losses, with a value of 2 typically assumed [4]. To achieve such velocities, a generator must be able to drive a voltage [5]:

$$V_{load} \sim I\dot{L} = I\frac{\mu_0 l}{2\pi}\frac{d}{dt}ln\frac{r_f}{r_t} \sim \frac{\mu_0 I l}{2\pi r_f}\sqrt{\left(\frac{4.048Z^{3.6}}{A}\right)}$$

For efficient thermal K-shell emission from Mo at 17 keV and Ag at 22 keV, respectively, the required voltages are 7.7 MV and 9.0 MV - larger than present few-MV-scale capabilities.

While thermal K-shell emission requires a significant investment of internal energy to reach the K-shell, cold Kα line emission can be produced from more recombined ions in much cooler material by the 2p-1s decay that follows inner-shell ionization. Using existing machine voltages (which are insufficient to provide efficient thermal K-shell emission) to directly accelerate electrons to T_{hot} ~ 100 keV could thus produce intense inner-shell emission with only a weak dependence on material Z, that is $\exp(-10Z^2/T_{hot})$. This is similar in spirit to the last decade's investigation into Kα generation from ultrashort, high-intensity laser sources, which generate fast electrons that can directly produce inner-shell emission without ionizing material to the K-shell[5]. Non-thermal Kα emission has been observed on previous z pinch experiments on Z[6] and smaller generators[7]. It is generally a signature of non-thermal and/or non-local effects in plasmas because it requires high-energy particles (photons or electrons with energies higher than the 1s photoionization threshold) interacting with cool plasma regions.

We have experimentally studied a number of important factors in developing a Kα source on Z. To investigate the scaling of these non-thermal sources, experiments have been performed with Mo and Ag wire arrays and past data with lower Z materials has been reexamined.

To illustrate the scaling of thermal and non-thermal emission with atomic weight and photon energy, we present data from four experiments, with materials from stainless steel to silver, as shown in Figure 2.

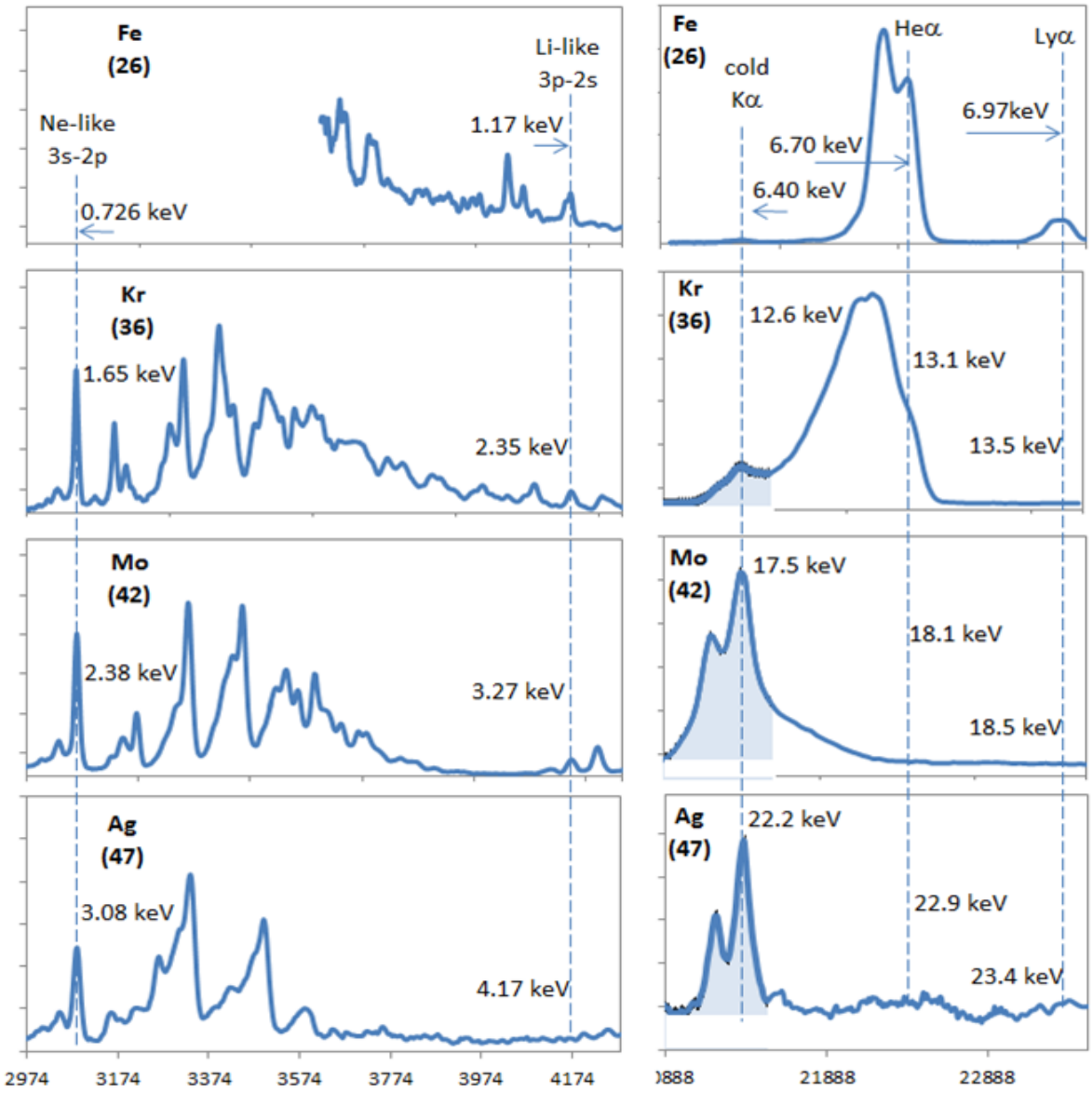

Figure 2: Change in L-shell spectrum (left) and K-shell spectrum (right) for different wire array materials from Fe (top) to Ag (bottom).

First, we show the results of z2501, typical of the optimized stainless-steel wire array platform[8]. These 70 mm-diameter, 2cm tall nested wire arrays with total 0.7 mg/cm mass (divided 2:1 on the outer and inner arrays) reliably produce 70 kJ of K-shell x-rays in a few ns with average energy around 7 keV, near the Fe Heα energy of 6.7 keV. Next, we show data from z2543, a recent Kr gas puff shot that used new 31 cm convolute and the largest load diameters ever fired on Z, with a 120-mm-diameter outer jet and a ramped mass profile with a total of 0.67 mg/cm over 2.5 cm in height, designed using the Gorgon code to produce large kinetic energies to drive a high-temperature plasma at stagnation[9]. Finally, we show data from two additional

nested wire arrays, both with 50 mm diameters, 2:1 outer:inner mass ratios and 1.3 mg/cm linear mass. Shot z2533 used pure Mo wires[10] and shot z2535 used an Ag/Cu/Au (70/20/10) alloy[11].

All four shots were diagnosed with suite diagnostics including photoconducting diodes[12] and spectrometers to measure the absolute emission yields, duration, and spectroscopic distribution of the emitted x-rays. The time-integrated spectrometers included a pair of cylindrically-bent crystal spectrometers (TIXTL[13]) with KAP providing spectral coverage from ~1-8 keV and LiF providing coverage from ~4-24 keV, both axially resolved. Additionally, we fielded the compact, rugged in-chamber transmission spectrometers (CRITRs[14]) which provide ~7-25 keV spectral coverage with both radial and axial resolution. This set of spectrometers has been semi-empirically absolutely calibrated[15] to about 50% accuracy.

The shift in spectrum from the thermal K-lines to the cold Ka line can be seen directly in the spectra. Figure 2 shows the progression of experimentally obtained spectra for metals from Fe to Ag. As the atomic number is increased, and the ionization energy required to ionize to the K-shell increases, the non-thermal Kα line becomes increasingly dominant. This is consistent with observed trend in the L-shell spectrum, which indicates a decrease in the ionization state of the pinch with increasing atomic number, from few-electron Li- and He-like ions for Z = 26 to ~10-electron Ne-like ions for Z > 40.

Figure 3 shows a summary of the yield scaling of thermal K-shell lines and non-thermal K-shell lines for metals from Al to Ag. Shown in blue is the scaling of the Heα line yields. As expected, with increasing atomic number (and hence photon energy) the yield radiated in the Heα line decreases considerably, and is well represented by a typical electron temperature of ~2.5 keV. For the non-thermal cold Kα line, associated with inner-shell ionization and shown in green, the scaling is much flatter; dominating over the Heα emission for Z > 40. The trend in cold Kα emission is consistent with the presence of higher energy electrons, and the scaling can be recovered assuming a 60 keV monoenergetic electron population (although this is by no means a unique solution).

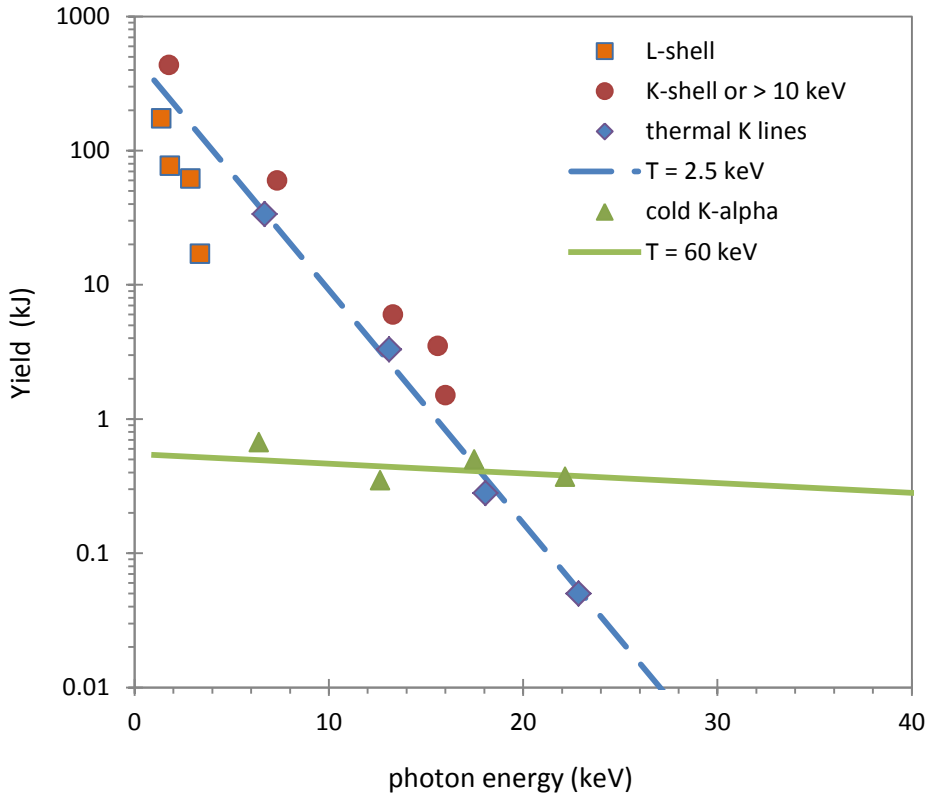

Figure 3: Scaling of thermal and non-thermal line emission with material and photon energy.

2 DIAGNOSTIC DEVELOPMENTS

2.1 Overview of diagnostic developments

The Z generator has an extensive suite of diagnostics tailored to characterizing soft/cold x-rays (<15 keV). These include diagnostics that are routinely used to characterize the yield, spectrum and pulse shape produced by radiation sources. These diagnostics are complemented by a range of other diagnostics that help provide data on the implosion dynamics and temporal evolution of the emission for these sources, helping provide physical understanding of the x-ray sources. The effectiveness of many of the traditional diagnostics on Z is limited to <20 keV due to both the drop in response of detectors and the drop in source yield at high energies.

In parallel with efforts to push x-ray source on Z to higher energies, it is equally necessary to develop x-ray diagnostics that are able to characterize these x-ray sources. As such we have developed a suite of diagnostics targeted at characterizing the fluence, spectrum and pulse shape of warm x-ray sources on Z. Additionally, in order to aid in the understanding of these warm x-ray sources we have developed a diagnostic for characterizing the spatial structure of emission in warm x-ray sources and also to characterize the energetic electrons present in a z-pinch plasma.

2.2 Yield/fluence using TLDs

To provide data on Yield and fluence at >20 keV we have developed a diagnostic based on differentially filtered thermoluminescence detectors (TLDs), as shown in Figure 4a. These TLDs, which have long been used as a diagnostic on other facilities, provide a calibrated fluence measurement. Filters can be selected to provide either an effective bandpass using Ross filter pairs (Figure 4b) or a broad range of materials can be used to characterize broadband Bremsstrahlung radiation (Figure 4c,d). Combining these broadband measurements with other diagnostics of the Z facility enable broadband characterization of the radiation environment, as illustrated in Figure 4d.

Further details of the TLD diagnostic developed for Z will be discussed in more detail in a future SAND report.

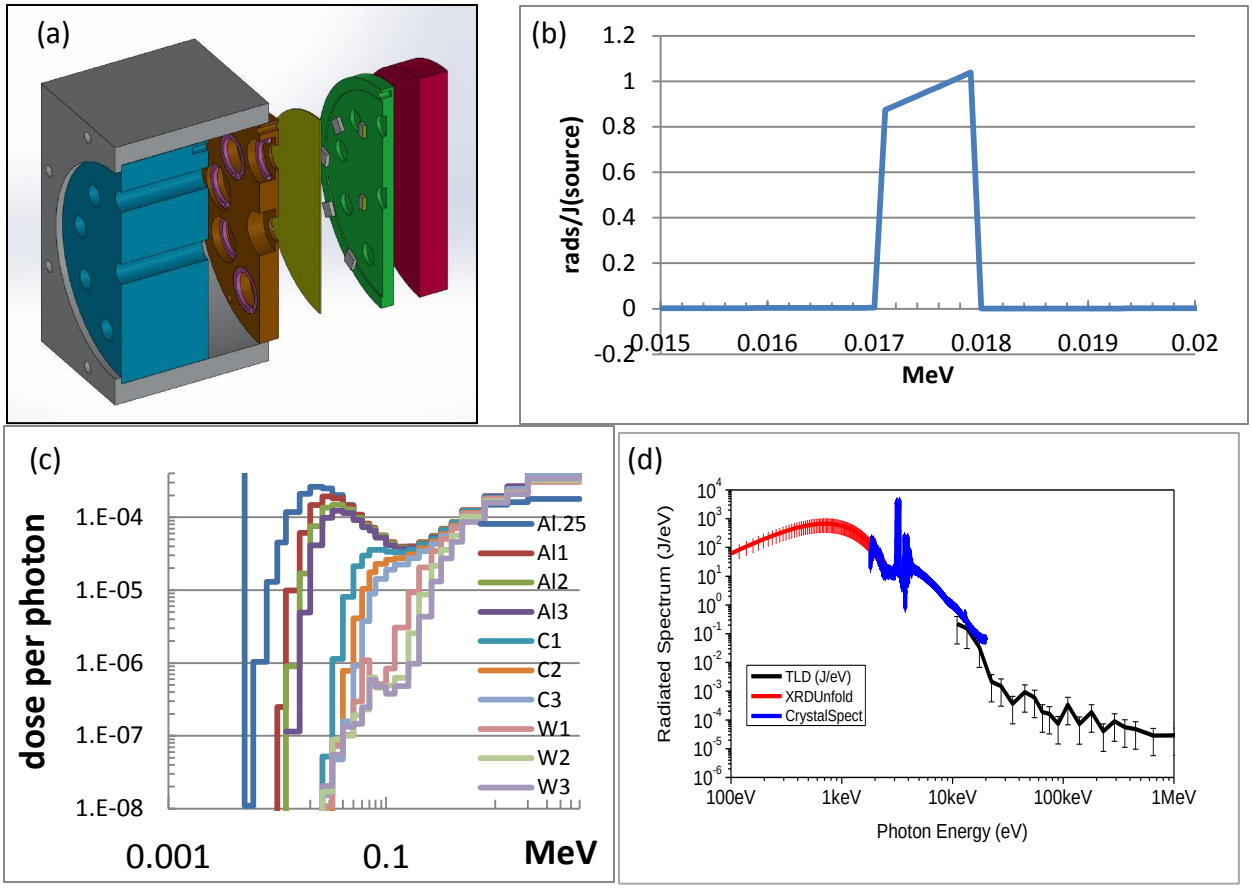

Figure 4: TLD based diagnostic. (a) Instrument setup and (b) transmission window from the subtraction of a Ross filter pair. (c) Filter setup for Bremsstrahlung characterization, and (d) spectrum unfolded from TLDs (black) combined with other data to provide broadband source characterization. Initial unfolds are shown here to be indicative of the capabilities of this instruments, and are not a definitive analysis of the data.

2.3 Spectrum using CRITR-X[19]

An upgrade of the Compact Rugged In-chamber TRansmission spectrometer CRITR spectrometer[14] was designed, developed, calibrated and implemented at the Sandia Z facility[a]. This upgrade, called CRITR-X, complements the existing suite of Z diagnostics to photon energies higher than 25 keV and up to about 100 keV.

The applications of CRITR-X are similar to those of the CRITR instrument but extend the range of Z sources emitting hard x-rays provide absolutely calibrated measurements (a significant improvement over the original CRITRs). In particular, to the CRITR-X instruments have been critical for measuring non-thermal z-pinch emission from Mo (17 keV), Ag (22 keV), W (60keV) and Au (70 keV) and continuum bremsstrahlung radiation hν≥ 12 keV.

2.3.1 Design improvements implemented in CRITR-X

The CRITR-X is an upgrade of the CRITR instrument[14], they share the same geometrical concept with x-rays nominally following the same paths in the two instruments. For both instruments, the dispersion is obtained through the Laue diffraction of x-rays by a cylindrically bent crystal according to the Cauchois spectrometer geometry[16]. The Cauchois geometry is the most efficient geometry for crystal based spectrometer at such high energies and has been implemented successfully on several high-energy-density facilities[17],[18]. Both instruments share the same in-chamber housing making the implementation of this upgrade on the Z facility transparent compared to CRITR. The 1D slit imaging capability uses the same principle as the in the CRITR instrument, except for the difference that the expected spatial resolution is of about 500 μm limited by the slit size that can be effectively built at such high photon energies.

The upgrade improves upon the existing CRITR through the following points:

- The main hardware components were entirely designed using previous extended experience from Artep Inc.. The new design include kinematic fixtures for both the crystal assembly and the detector to allow higher accuracy in the placement of the these critical elements. In addition crossover slits to limit the collection of rays going to the detector and thus reducing background were designed.

---

[a] This spectrometer was developed for both LDRD 117862 and a Grand Challenge LDRD (173104). The design and fabrication was provided by the Artep company. The absolute sensitivity calibration was performed in collaboration of Artep, Sandia and the NIST using facilities at the NIST. A Sandia employee (G. Loisel) participated in the acquisition and processing of the absolute calibration data as well as in developing the fundamental physics of the instrument to provide a high level of understanding and a quick model to perform the data processing of collected Z data.

- The set of crystals was extended to increase the spectral range to 6-100 keV so extending above the 25 keV CRITR current limit. Over this extended range the sensitivity was required to be of at least 10 J/eV/cm at the source while maintaining a reasonable spectral resolution, $\lambda/\delta\lambda \geq 200$
- The instrument also comes with an absolute crystal sensitivity for all available instrument configurations to about 5% accuracy.

2.3.2 The CRITR-X spectral range

The extended spectral range 6-100 keV is obtained by interchanging crystals in the instrument. The different crystals have different lattice spacings, thus providing shifted and overlapping spectral ranges according to the Bragg's law of diffraction: $n\lambda = 2d \sin(\theta_B)$ with λ the diffracted wavelength in order *n*, *2d* is the *2d*-spacing of the crystal cut and θ_B is the Bragg angle, angle of incidence of diffracted x-rays on the crystal lattices.

The crystal cuts are taken from a quartz boule. Each cut, designated by its Miller indices, is chosen based on its *2d*-spacing that is the primary control of the spectral range and also keeping the cut efficiency high enough. Table 1 gives the list of elected quartz cuts that can be fielded in CRITR-X and the corresponding spectral ranges. The crystals are bent to a radius of 250 mm; this bending radius is a compromise between obtaining a large set of Bragg angles on the crystal versus the limitation on how much a crystal can be bent with keeping a good crystal quality.

An analytical model of the dispersion was derived and matches the numerical ray-tracing to within machine precision. This analytical model allows for an accurate determination of the photon energy axis on the recorded data through the optimization of a few main geometrical parameters of the instrument with the goal of matching observed photon energy dependent fiducials in the data. This will be presented in a separate publication.[19]

Table 1: Description of the CRITR-X quartz crystal cut, spectral ranges and relative efficiencies ϵ in % for different orders, noted ϵ (n) for the nth order. Relative efficiencies are given relatively to the (101) cut in 1st order and calculated using the XOP code[20].

Quartz cut (Miller indices)	*2d-spacing (A)*	*Spectral range (keV)*	*ϵ(1)*	*ϵ(2)*	*ϵ(3)*
101	6.68	7-25	100	19	12
203	2.75	16-51	54	7	0.2
502	1.62	28-100	23	4	1

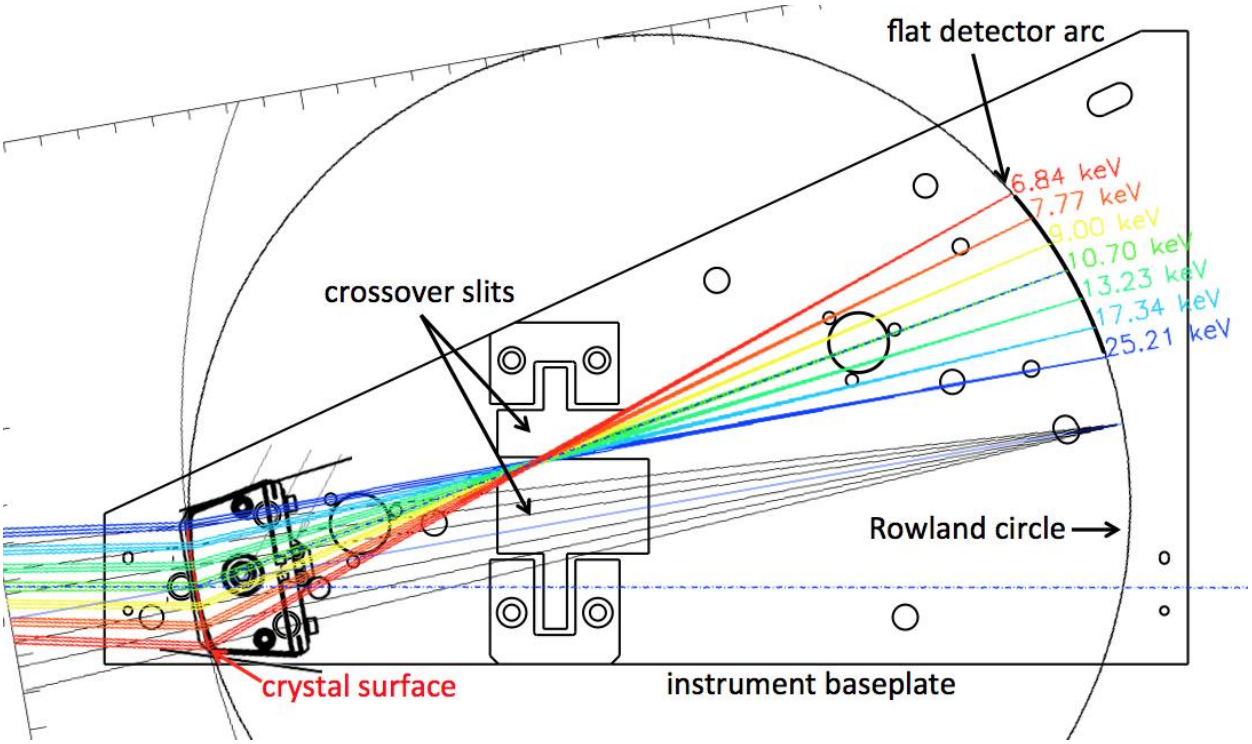

Figure 5: Dispersion plane view of the CRITR-X baseplate and ray-tracing. The x-ray source is located outside the figure on the left. The source spectrum is dispersed by the transmission Laue crystal (red arc) and is recorded onto the detector, each color corresponds to one photon energy as indicated at the location of the detector. On average, rays deviate with 20° from the original source-instrument sightline direction. This has the benefit of shielding the detector from non-dispersed stray light coming straight through along the instrument line-of-sight.

Figure 5 shows the dispersion plane of the instrument and how photons with different photon energies are dispersed to the detector. The ray-tracing is overlaid to the CAD drawing of the instrument baseplate. On this figure one can see that an extended monochromatic source in the dispersion plane will be focused on the Rowland circle, making the Cauchois geometry particularly efficient at collecting spectra.

2.3.3 The photometry of CRITR-X: modeling and calibrations

The photometry of the CRITR-X can be described with the efficiencies of its basic components, namely:

1. The bent crystal efficiency: In Cauchois geometry the dispersing element is a bent crystal used in transmission. Its efficiency is properly described with the theory of Laue diffraction of x-rays by crystals. The efficiency is encoded in the so-called integrated reflectivity R_{int}, that represents the crystal reflectivity of the crystal integrated over small range of angles about the Bragg angle $\__B$. Its use is described in the next geometrical efficiency term. There exists several model to calculate the integrated reflectivity of a Laue crystal. This quantity is in general difficult to model accurately, especially for bent crystals. Calculations show typically a factor of a few difference with calibrations, although there are more reliable in a relative sense [9], relative with respect to photon energy (accurate shape) or relative from one order of diffraction

to another at a given photon energy. The extension of the project would be to develop a better modeling of crystal efficiencies and is outside the scope of this document.

2. The instrument geometrical efficiency*:* The geometrical efficiency includes the bending of the crystal, distances in play in the instrument, the instrument dispersion, also the attenuation through the crystal. The total geometrical efficiency that converts exposure on the detector in photons/cm^2 to source intensity in J/eV/sr is given by:

$$\epsilon\ ([\mathrm{ph/cm^2}]\ /\ [\mathrm{J/eV/sr}]) = \frac{H}{W(H+F)}\frac{d\lambda}{dx}\Omega_{\mathrm{eff}}$$

H is the source to crystal distance, *F* is the crystal to detector distance, *W* is the crystal width, *dλ/dx* is the instrument dispersion in units of wavelength per film position (Å/cm) and Ω_{eff} corresponds to the instrument throughput, i.e. the effective solid angle subtended by the area on the crystal that effectively diffract a given photon energy and as seen from the source. The throughput includes the photon energy dependent crystal response R_{int}. All terms in this equation are photon energy dependent.

The throughput Ω_{eff} can be written as:

$$\Omega_{\mathrm{eff}} = \frac{W}{H^2} r_c \sin\theta_B R_{\mathrm{int}} \left\langle \frac{d\gamma}{d\theta} \right\rangle$$

with r_c the crystal radius of curvature and the last term $\langle d\gamma/d\theta \rangle$allows for the conversion of the integrated reflectivity as measured in a typical rocking curve measurement into a mean reflectivity using the instrument angular coordinate γ defined as the angle of the incident x-ray with the instrument line-of-sight. The detailed derivation of these results will be published elsewhere[19]. The geometrical efficiency Ω_{eff} is shown on Figure 6 for the (101) and the (203) crystal cuts.

3. The detector efficiency*:* Nominally the detector of choice is Imaging Plates (IP), which spectral response was calibrated by Meadowcroft *et al.*[21]. This response is in fact dependent on the specific IP type and the scanner used to scan the IP. Therefore the specific scanner used to scan the Z data needs also to be calibrated.

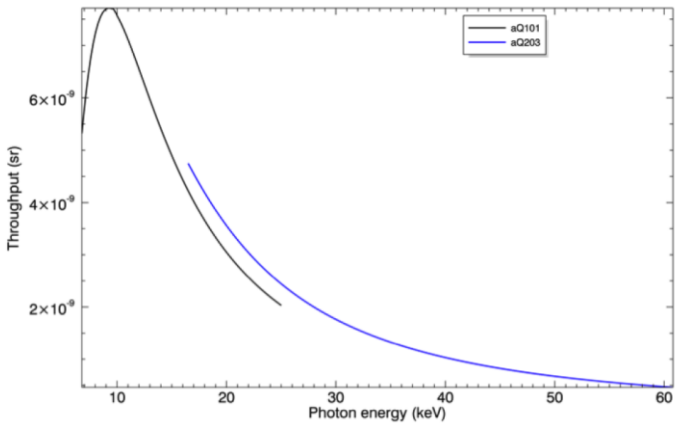

Figure 6: The efficiency for the (101) (in black) and the (203) (in blue) crystal cuts. Below about 10 keV the efficiency drops because of an increase in absorption by the crystal as the photon energy decreases.

2.3.4 Photometry calibrations at the NIST air KERMA facility

The NIST air KERMA facility generates spectra absolutely calibrated with 4% relative uncertainty in narrow selectable energy bands. Each band spectrum is part of international x-ray source standards and are routinely used to calibrate x-ray detectors. The source is a 100kV tungsten tube coupled to a filter wheel with adjustable voltage to create a narrow spectrum with the lower photon energy cut-off is given by the filter and the high energy cut-off is set to the running source voltage. Figure 7 shows the facility and calibration setup (left) and the set of used standard beams (right).

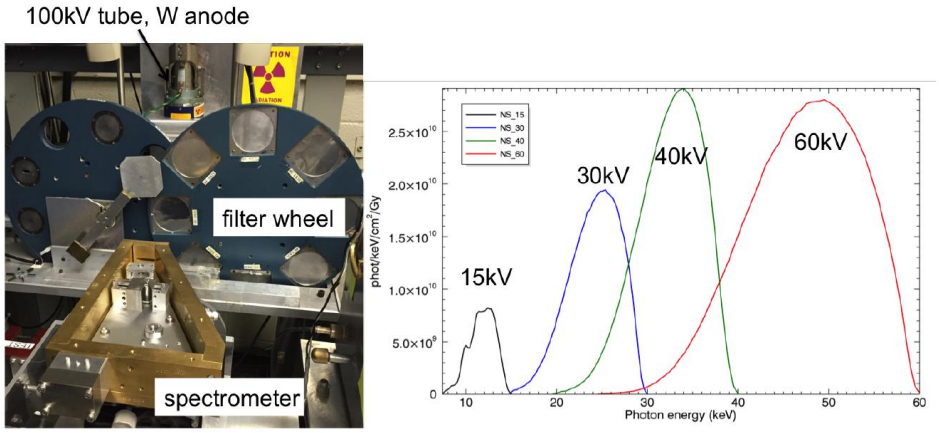

Figure 7: The NIST air KERMA facility. (left) Picture of the calibration setup including the x-ray source, filter wheel, and the spectrometer. (right) the absolutely calibrated (4%) spectra from the source, the combination of source voltage and filter defines a narrow band spectrum indicated by the running voltage in the plot.

The photometric model presented previously is tested against the calibration data. We recognize first that the crystal efficiency model could be off in an absolute sense, such that only the spectral shape is assumed accurate, the comparison with calibration data is then performed with one scaling factor adjustment.

Figure 8 shows such comparison for the (101) and the (203) cuts and for two source beams for each crystal cut. The calibration data was processed following the efficiency responses described earlier after calibration of the photon energy axis, thus converting the detected signal into a an absolute spectrum from the source.

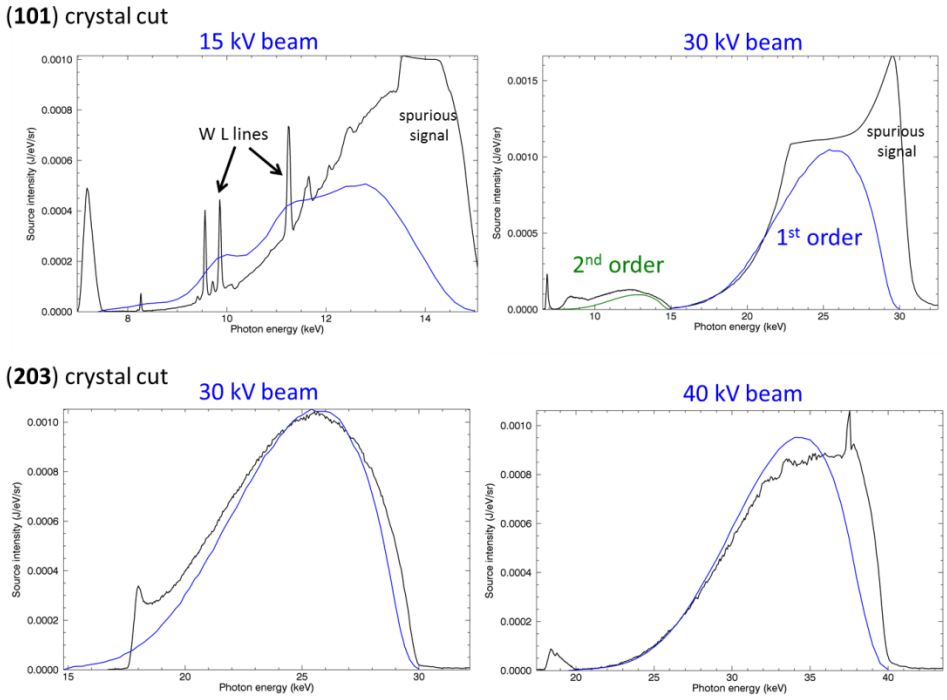

Figure 8: Comparison of the calibration data with the photometric model. The top plots are for the quartz (101) cut for two different source beam, the beam voltage is indicated on top of each plot. In each plot, the calibrated source spectrum is shown in blue while the measurement unfolded from the photometric model. For the (101) cut, a spurious extra signal was recorded on the high energy side that was probably coming from extra scattered signal, this side of the spectrum is therefore neglected when using the calibration data.

As can be seen from the figure a reasonable agreement is obtained when using a constant scaling factor of 5.2 for all measurements. This scaling could easily be attributed to the inaccuracy in the absolute crystal efficiency calculated response. This scaling factor will be used to apply the absolute instrumental response on shot data, relying on these calibration data.

The absolute calibration is presently estimated to be accurate to about 10-20%, this value will be scrutinized as the full calibration data will be convolved together and error propagated. A 5% accuracy in crystal efficiency has been obtained in a separate work[22].

2.4 Spatial structure – Time Integrated Pinhole Camera (TIPC[23])

A pinhole camera has recently developed targeted to measure >15 keV photons[23]. As with other diagnostics for this spectral range, this instrument sits within the main vacuum chamber of Z to maximize incident fluence. Five images are produced on each shot by a set of five 250μm conical pinholes in a 1-cm thick W plate, which can be independently filtered to provide five spectral responses. The five images are recorded on image plate.

To complement our understanding of non-thermal z-pinch emission, we have developed setups for this instrument and developed processing techniques to provide a band-pass image. The diagnostic is fielded with differential filter pairs with similar transmissions in regions other than the region of interest, hence the subtraction of the two images is effectively a band pass image of the spectral band of interest.

Figure 9 shows raw images recorded by this image with two different filter cuts (left two images, the filters are shown in the plots) and the difference between these images, which represents an image exclusively from the 17-20 keV spectral band.

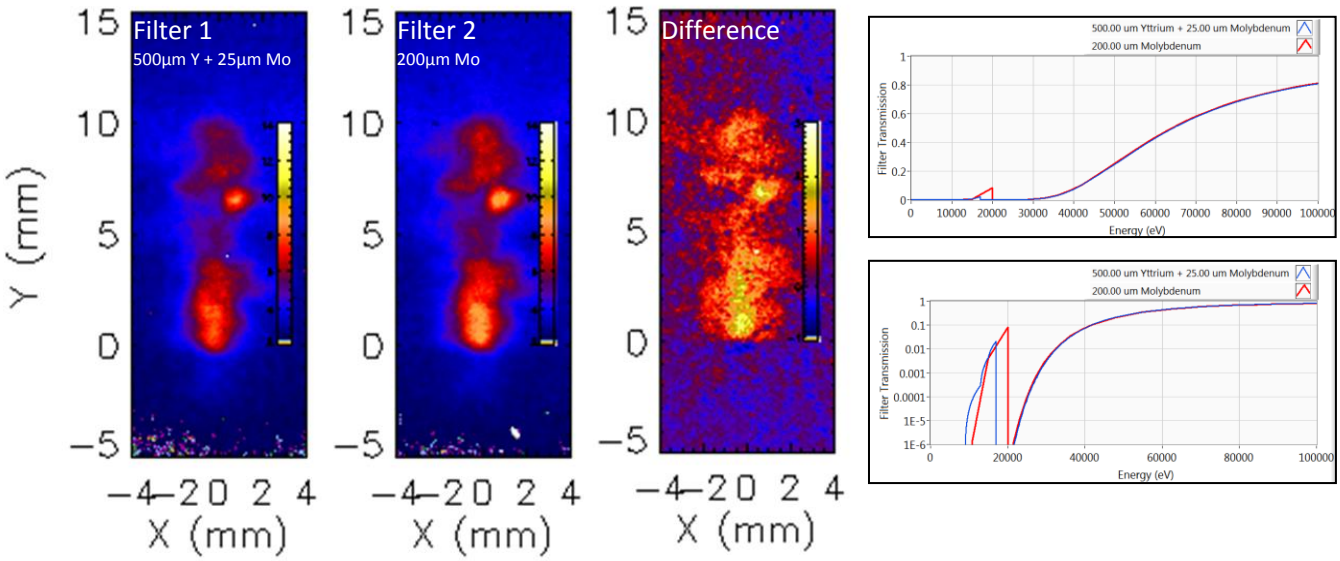

Figure 9: **Differentially filtered images, with the filter transmissions shown in the two plots. Subtracting these two images provides a bandpass image as shown.**

2.5 Faraday Cup

We have developed a novel diagnostic with the goal of measuring electron beam currents originating from the z-pinch of the imploding wire array. As previously discussed, hot electrons are one of the mechanisms for generating non-thermal K-shell x-rays from the stagnating Z-pinch. The energy distribution and magnitude of the electrons are not known precisely though the timing is expected to correspond closely to peak non-thermal x-ray emission. Simulations of the electrons showing the spatial distributions and trajectories do not show a strong preferential direction, or in other words, a directional beam may not be produced. Therefore we put the detector aligned to the z-axis, above the array, with the purpose of sampling these hot electrons.

The diagnostic consists of an array of Faraday cup electron collectors with the option of flat-foil filters of various thicknesses in front of the cup apertures. There are also a series of electron current monitors consisting of B-dot (magnetic field pick-up loops) located in a drift region below the Faraday cups. The combined assembly is shown in Figure 10.

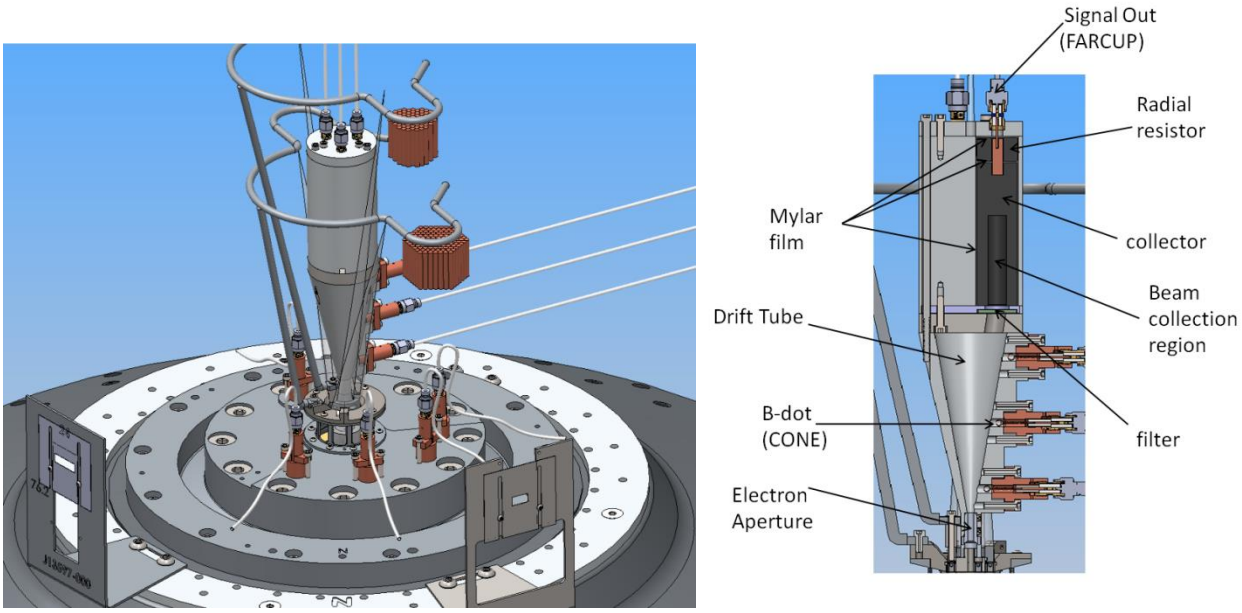

Figure 10. (Left) Wire array faraday cup diagnostic as fielded above the load on Z. (Right) Internal structure of the Faraday cup diagnostic. The wire array is centered just below this figure. Only one of the three Faraday cups is shown in the top half of the device. For most shots the filters used for the Faraday cups where approximately 0.012 inches, 0.03 inches, and 0.06 inches stainless steel.

The theory of operation is as follows. There is a 0.11 inch aperture directly above the center of the wire array upon which the electron "cloud" from the pinch is incident. A narrow beam of electrons should be produced, traveling upward, with a high degree of randomized directionality which should result in a broad, uniform current density in the conical drift region. Each b-dot current monitor sees the magnetic field from the beam and allows a total current measurement in the drift region. Hopefully the electron beam disperses rapidly. A uniformly-distributed beam across the upper region of the drift tube where the Faraday cups are located

is a critical characteristic in order to quantitatively interpret the Faraday cup signals as will be explained shortly. If the each B-dot current monitors a decreasing electron current as a function of distance away (upward) from the aperture in the drift tube, then there is good reason to expect that a uniform beam is being created by an expanding beam since some current is being lost to the walls of the drift tube. Ideally we would like some verification that a uniform beam is incident on the end of the drift tube, but this would likely require some form of imaging diagnostic which does not exist in the application at this time.

At the top of the drift tube, there are three separate Faraday cups. The device is based on a design from Reference 24. The Each Faraday cup consists of two main components (not including the filter foil considered in a moment). There is a carbon collector with a deep (large depth-to-radius ratio) hole into which the electron beam is incident. The collector is low atomic number to minimize secondary electron emission which would reduce the signal; however, the aperture is present to minimize the effect of any secondary emission since the secondary particles would be unlikely to escape the aperture of the collection region. This feature eliminates the need to bias the Faraday cup. Beam current travels to electric ground through a radial resistor also made of carbon (graphite). This resistor is placed very close to the collector to minimize the circuit inductance. The beam current is therefore simply the measured voltage divided by the resistance of the radial resistor. It is important to note that the Faraday cup is not hardware or software integrated like the B-dots to get the current. The voltage signal is measured by a 50 Ω coaxial cable with the center conductor attached to the center of the radial resistor. The resistance of the radial resistance must be much less than the coaxial cable impedance in order to drive most of the current through radial resistor and not the cable. The collector and radial resistor is electrically insulated from each other and ground except for the required current path by Mylar film. The resistance of the radial resistor must be also low enough to avoid high voltage breakdown in the Mylar but large enough to generate a sufficiently strong signal from the beam current.

Filters are placed at the upstream side of the Faraday cup collectors. It is important that they are electrically isolated from the collectors in order to not short out the Faraday cup. The thicknesses of the filters are set to stop electrons below a certain energy from passing through it. For these tests, a thickness corresponding to the CSDA range[25] for electrons in stainless steel was chosen for the energies of 0.5 MeV, 1.0 MeV, and 2.0 MeV. However, the filters actually attenuate the beam with all energies above these limits. Example beam attenuation for 3 MeV electrons through aluminum is shown in Figure 11. Therefore without further numerical analysis (see next section), a measured Faraday cup signal only indicates that beam greater than the threshold energy is present.

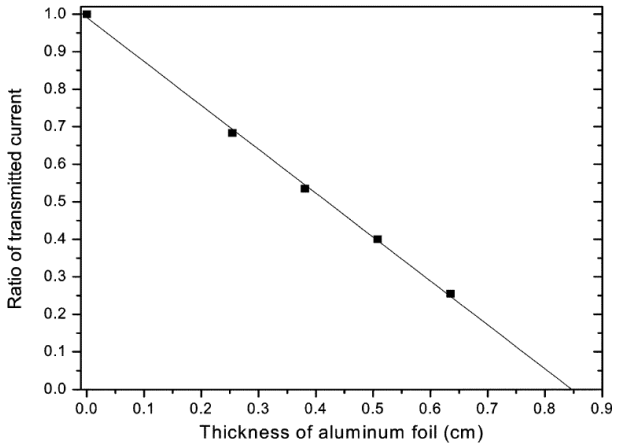

Figure 11. Calculated electron beam transmission through aluminum for 3 MeV.[26]

The Faraday cup design was used on a number of Z shots (includes 2654, 2655, 2656, 2657, 2658, 2751, 2775, 2776, 2777, 2823, and others including later shots). Many of the shots did not result in useful signals on some or all of the signals. For later reference, the drift tube B-dots are referred to as CONE (with numbers 5-7 from the bottom to the top) and the Faraday cup as FARCUP (numbers 8-10). In some cases the signals were completely uniformly-distributed noise. The CONE signals were highly susceptible to a large signal that appears to be associated with the Z load current. It is likely that the magnetic field from the current flowing in the load is able to be partially detected by the CONE B-dots. In many of the instances, a signal that appears to be associated with real drift tube current is perceptible above this long-time-frame external background, but it is difficult to extract the desired drift tube current because the external background appears to be different for each of the CONE B-dots. A metallic filter at the entrance to the drift tube may be successful in blocking this external current pickup.

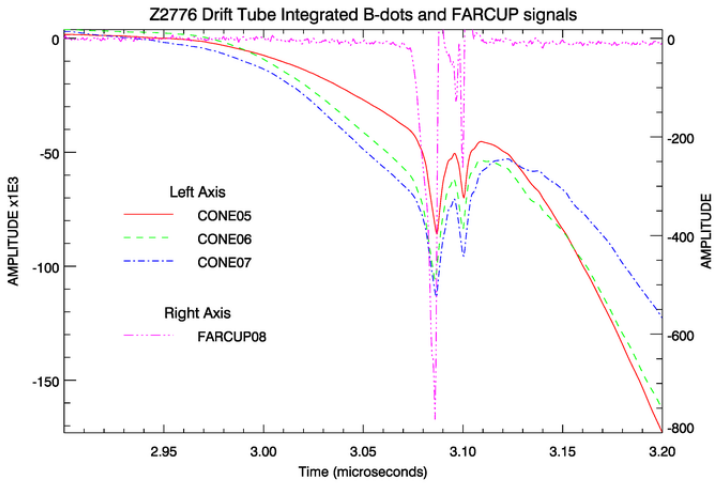

Figure 12. An example of CONE signals and a Faraday cup signal. The gradually ramping current is most likely due to the load current magnetic field being detected by the CONE B-dots. However there is a fast pulse on top of the background signal which occurs at the same time as the Faraday cup signal which is likely due to the electron beam in the drift region.

The FARCUP signals appear relatively clean (either they generate a clear pulse or they are complete noise). Unfortunately, individual calibrations of each of the Faraday cups were not achieved though it is straightforward to design a fixture to do an absolute calibration, similar to how B-dots are calibrated. Barring a calibration, we must assume that the Faraday cups are all built identically with the same resistance (this can only be true to some level, now unknown). As a check of the combined uniformity of the electron beam spatial distribution and the Faraday cups themselves, a "flatfield" shot was performed (Z2751) where an identical thickness of filter was used. The FARCUP signals are shown in Figure 13. The signals appear to be the same within about 10% which is acceptable. A shot where different thicknesses of filters were used is shown in Figure 14 (Z2655). Full disclosure: there is some ambiguity as to which filter went with which signal on this shot; normally it is #8, #9, and #10 from thin to thick, but we assume it went the other direction based on the signal amplitude.

There is some difference between the time of peak x-ray emission as seen by the x-ray sensitive photo-conducting diodes. In general, the FARCUP signals are later than the PCD signals by a few tens of nanoseconds and sometimes less depending on the shot (the FARCUP signals are all well time synchronized to within 1 ns). For example, in Figure 15, the PCD comes about 15 ns earlier than the FARCUP signal; another shot, Figure 16, shows them being much closer. It has yet to be determined if this is a signal-acquisition or processing error, time-of-flight difference, or some other effect. The CONE signal channels also show current of similar width at this same time (Figure 4); the large-amplitude external pickup referred to earlier happens over a much longer time frame. There were several other shots that gave FARCUP signals at the right time, but with relative amplitudes not in accordance with the filter that should be placed on the particular Faraday cup.

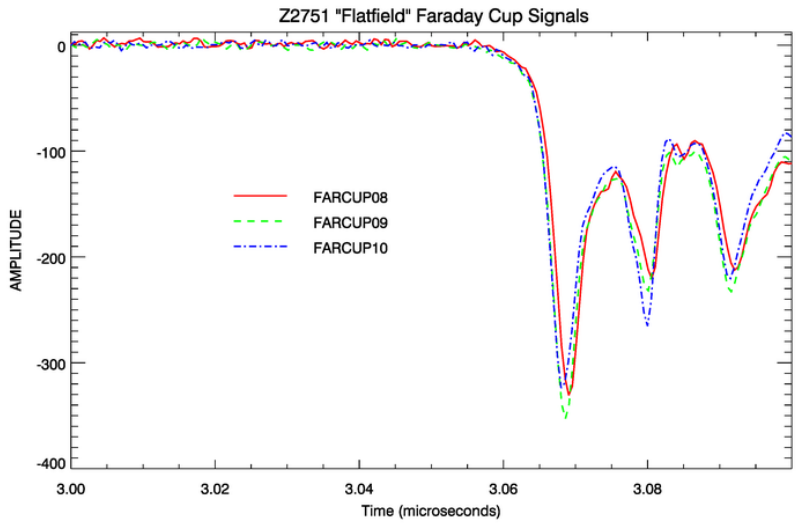

Figure 13. Faraday cup signals on a shot where an identical filter thickness was used on each channel. Since the signal amplitude was very similar, this indicates that the electron beam current density was uniform and Faraday cup has the same calibration.

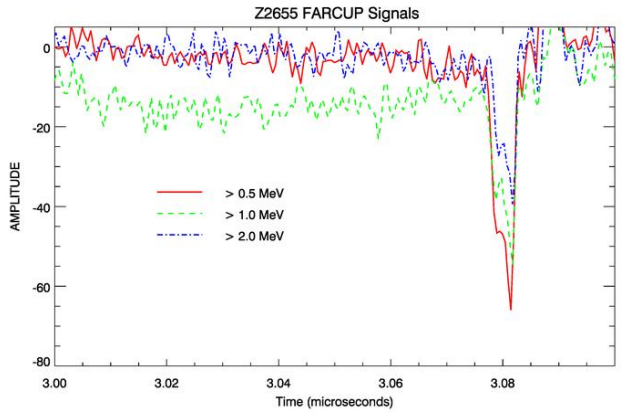

Figure 14. A shot where different thicknesses of filters were used on each of the Faraday cup channels.

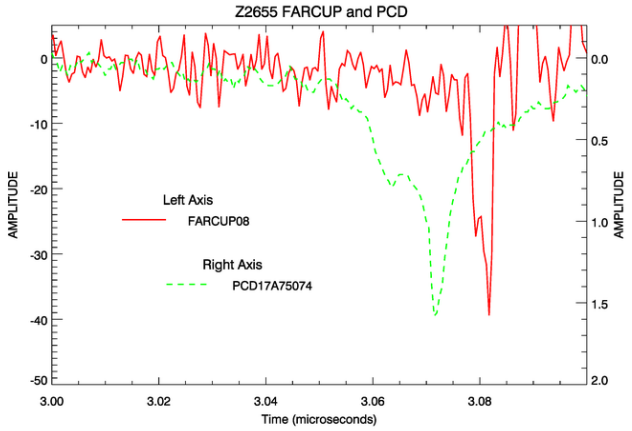

Figure 15. Timing of the PCD and Faraday cup signal on a shot.

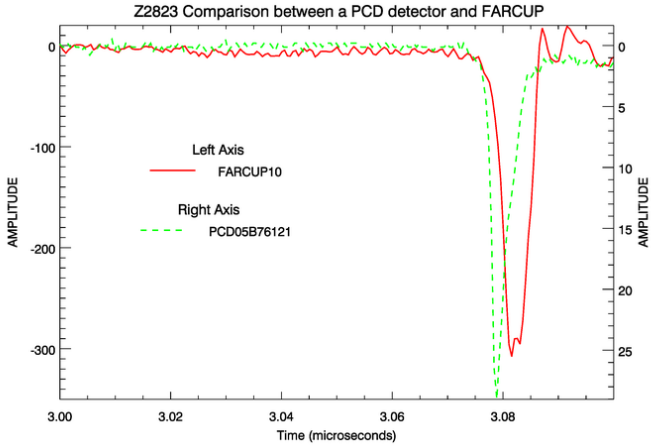

Figure 16. Timing of the PCD and Faraday cup signal on another shot.

The wire array Faraday cup diagnostic is designed for electron beam current measurements to give an idea of the lower bounds of the electron energy distribution. The FARCUP signals have approximately the right shape in comparison to time-resolved x-ray photodiode measurements that give some confidence that a relevant signal of the electron beam is being measured though some discrepancy in timing needs to be examined closely. Given the Faraday cup filter thicknesses used, there is strong evidence of an electron beam exceeding 2 MeV that comes from the z-pinch at the time of peak x-ray power. Quantitative measurements on future shots will require individual Faraday cup calibrations. Improvements to the CONE drift tube B-dots that avoid the large external current (probably from the load current) may allow an absolute current density measurement.

The primary challenge of the interpretation of the signals such as in Figure 6 is to identify any components of the signal, additive or otherwise, which may not be due to the hot electron beam originating from the z-pinch. Examples include plasma ions which may travel along with the electron beam or is generated within the diagnostic drift tube or in other locations. The CONE B-dots would be primarily affected by co-moving ions which may partially current neutralize the beam. The ions would not be able to penetrate the filters at the entrance to the Faraday cups, but the electron beam may be able to generate ions at the exit of the filters if they heat the filter sufficiently. We should be able to calculate the surface heating from the electron beam by knowing the electron current density and approximate energy at the entrance to the filters. It is also possible that the x-rays from the pinch may generate a signal within the Faraday cup due to secondary electron emission from surfaces within the device. This may be checked though simulation or measurement such as including a small dipole magnet at the entrance to the diagnostic to keep electrons away from the Faraday cups.

Once confidence is built that the Faraday cups are accurately measuring electron current, then analysis can begin concerning the energy distribution and consideration of further designs can commence. As currently fielded, the filters act basically as threshold filters in that electrons below a certain energy are blocked. However, the filters are highly imperfect in that they attenuate the beam of higher energies. As shown in the example in Reference 24, the beam attenuation is approximately linear with filter thickness. In order to determine the electron energy distribution, an unfold of the data considering the specific attenuators must be performed. A successful unfold will likely require many more data points (individual Faraday cups) with different attenuator thicknesses, preferably on the same shot. This would require a much larger surface area diagnostic to accommodate the number of channels. This is only a conceptual idea at this point, no designs or plans or ways to analyze the data have yet to be worked out.

2.6 Combining high-energy x-ray diagnostics

As discussed in Section 2, multiple x-ray imaging, power, and spectroscopic diagnostics are fielded on each Z shot. Taken together, they present a comprehensive set of data from which inferences can be made about the emitting plasma at stagnation. This picture can be used to constrain simulations and aid in the design of experiments to optimize desired outputs.

The principal power and yield diagnostic are filtered photoconducting diamonds (PCDs) and silicon diodes (SiD). Two types of SiDs are used on Z: small, thin diodes that measure lower-energy emission and larger, thicker diodes useful for recording high-energy emission (e.g. the DAHX differential spectrometer). All of these detectors record time-resolved voltages which can be converted to x-ray powers by first correcting the raw voltages V_r for the bias voltage V_b:

$$V = \frac{V_r}{1 - V_r/V_b}$$

then processing the corrected voltage V to give the power radiated into 4π:

$$P[W] = \frac{V\ \Omega\ d^2}{A\ R\ s}$$

with d the distance from the source to the detector in cm (1836, 249, and 729 cm for LOS 50, 170, and 210, respectively), R the resistance of the scope (50 Ohms is typical), $\Omega = 4\pi$ for an optically thin source, A the detector area in cm^2, and s the detector sensitivity to fully absorbed (low-energy) photons in A/W. A view-factor correction may also be required for 12° lines of sight (LOS 50 and 210): Assuming that the full source height h radiates with the same characteristics as the measured height h_m, the total power is obtained by multiplying the measured power by h/h_m. The total power here represents x-rays that pass through any filters and are absorbed by the detector. Since filter and detector responses are dependent on the photon energy, the shape of the source spectrum must be measured or assumed before absolute source x-ray yields can be assigned.

Cross-comparisons of PCD and SiD measurements help assess the uncertainty in yield measurements. While filtered PCDs have been standard power diagnostics for much of Z's history, the calibrated sensitivities of particular diodes range from 0.45×10^{-4} to 9×10^{-4} A/W – exhibiting significant variations from the nominal diamond sensitivity of 6×10^{-4} A/W. As part of this LDRD, a cross-comparison of SiDs with PCDs was performed, which indicated that the SiDs tend to have a uniform response to low-energy photons that is very close to the nominal sensitive of 0.268 A/W. The SiDs, however, appear to have a poorer temporal response than the PCDs, with good risetimes but few-ns tails that are currently under study.

Multiple spectrometers on Z cover a spectral range from ~800 eV to ~100 keV, as described above. The PCD and SiD measurements can be combined with measured time-integrated spectra to produce absolutely calibrated spectra that extend beyond the energy range of crystal spectrometer coverage, constrained by the signals of heavily filtered power diagnostics. An example of such a data analysis is shown in Figure 17, which shows a combined analysis of z2657, a conical Mo wire array. Emission spectra from the TIXTL spectrometers with KAP and LiF crystals were matched around 4 keV and then various high-energy tails were added to the spectrum above 20 keV. Using time-integrated PCD and SiD yields behind different filters, the absolute intensity of the spectrum and the energy dependence of the high-energy tail are both highly constrained. The inset figure shows a comparison of the yields measured by the power diagnostics (blue; solid from PCDs and open from SiDs) and those obtained from the calibrated spectrum (red). We find that a power-law tail best fits the high-energy data.

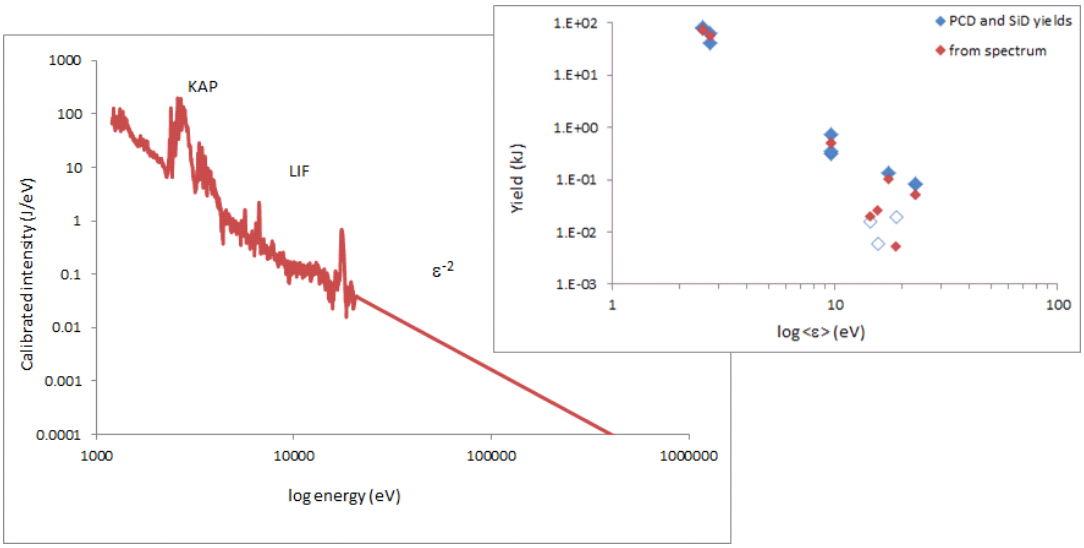

Figure 17: Combining high-energy x-ray diagnostics

3 DYNAMICS OF Kα EMISSION

Kα emission has long been observed to be emitted by wire array z pinches on various facilities, however little effort has bene put into understanding or optimizing that emission. In this study we have obtained data with a variety of setups which helps both understand the emission of Kα photons from wire arrays and explore the initial setups and stagnation conditions conducive to Kα emission. In this chapter we discuss data on the dynamics of Kα emission and then in the next chapter we discuss how this emission changes for different wire array setups.

The combination of diagnostics described above provides an extensive set of data that can aid in understanding the Kα production process and constrain the plasma conditions that produce the measured yields. Figure 18 shows a combination of a 17-22 keV self-emission image (a; obtained by subtracting images from the TIPC diagnostic) along with axially and radially resolved Kα spectra (b and c) and a filtered PCD trace (d).

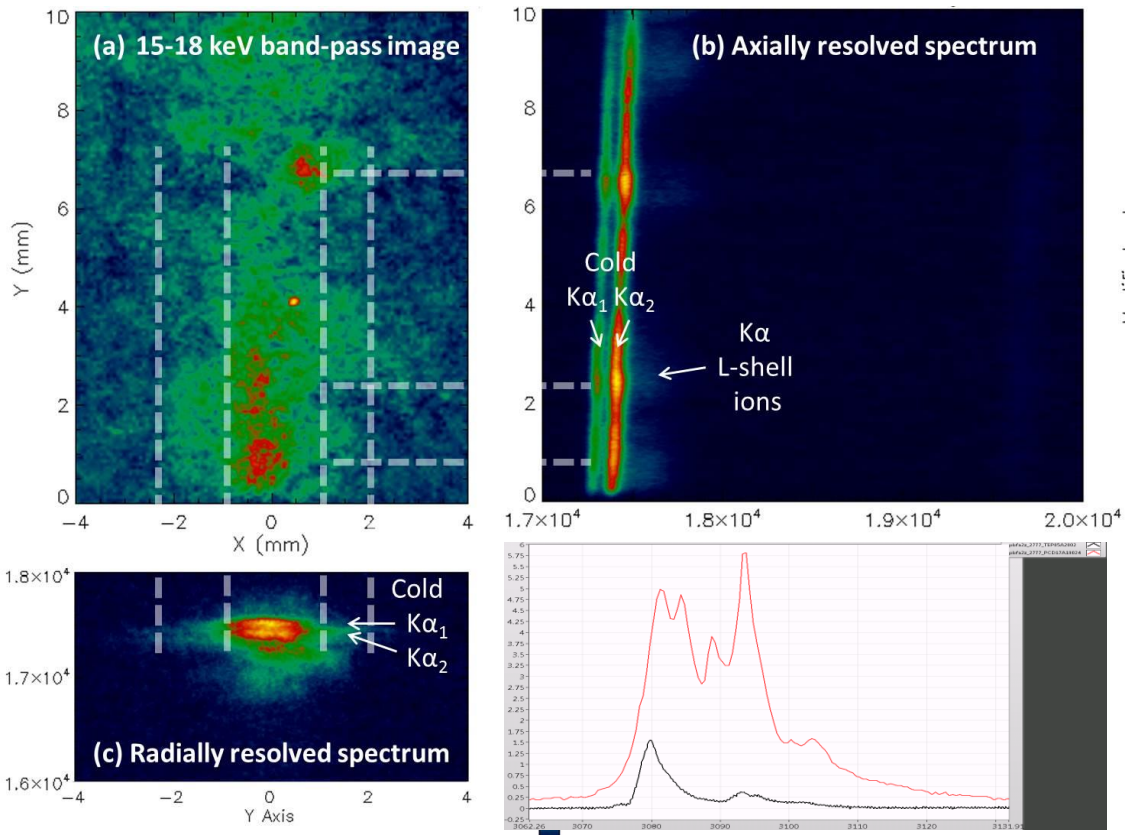

Figure 18: Structure in Kα emission, as shown by band-pass pinhole imaging (from image subtraction – see TIPC later) and from axially and radially resolved spectra. The structure is represents and unstable plasma column emitting Kα line radiation, which is consistent with the Kα radiation (shown in the red pulse shape) being produced late in the soft x-ray radiation pulse (shown in black)

From direct inspection of the data we can understand considerable information about Kα emission. The two-dimensional image, along with the axially resolved spectrum indicate that the emission is not uniform along the axis, and instead consists of brighter and darker regions. The two-dimensional image and radial spectrum indicate that the emission is broader than thermal K-shell in lower-Z wire arrays, such as stainless steel (few mm diameter here, ~1mm diameter in stainless steel).

The two-dimensional TIPC image in Figure 18c indicates that the emission is not from a uniform column, and instead is produced by a quasi-helical structure reminiscent of an m=1 (kink) MHD instability. This is typically observed in the disruption of a z pinch – on this Z shot imaging in softer photon energies indicates a more uniform was present before the pinch became unstable. Figure 18d shows PCD traces filtered for Kα photon energies (red) as well as for softer energies (black). This plot indicates that the Kα emission is after the peak of the soft emission, hence is consistent with he break up of the pinch.

As an example of the data analysis enabled by a dedicated study of the whole collection of data combined with detailed atomic modeling, we show a comparison 50 and 70 mm Mo wire arrays in Figure 19. Both arrays produced kJ-scale Kα yield, however the K-shell emission in the 70 mm case was dominated by interaction of energetic *thermal* electrons with hot L-shell ions in a ~1 mm core with Te ~ 4 keV, leading to Kα emission shifted to energies above the cold Kα. By contrast, in the 50 mm case the majority of K-shell emission was produced from non-thermal electrons interacting with cooler M-shell ions in larger (~ 6 mm), cooler region characterized by temperatures of ~2.5 keV. The larger-diameter, 70 mm array was designed to stagnate with high velocity and indeed appears to have produced a larger mass of hot plasma.

A comparison of the total modeled spectrum with the time-integrated data for the 70 mm array is given in the middle-right plot of Figure 19. Here, we see that the majority of measured L-shell emission and most of the thermal K-shell emission was produced in the initial stagnation. The high-energy PCD traces (top right) showed a smaller, post-stagnation peak, which we attribute to hot electron interaction with a cooler, larger post-stagnation plasma. By contrast, the PCD traces from the 50 mm Mo array showed a smaller initial (thermal) peak followed by a longer tail attributable to non-thermal electron interaction with post-stagnation plasma. On later shots where high-energy diagnostics were fielded, we found that the high-energy electron distribution was best fit by a power-law function.

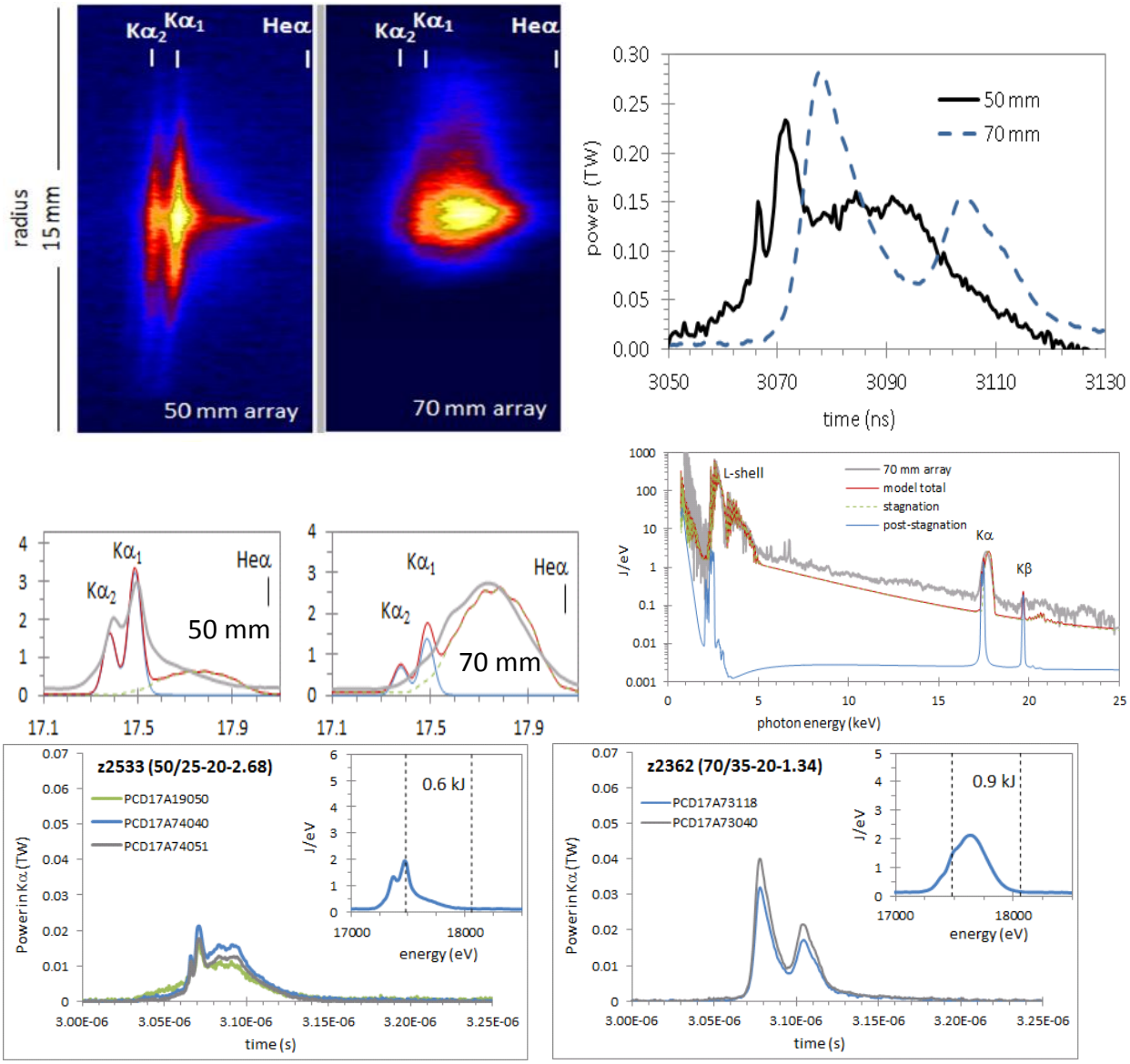

Figure 19: Left: Radially resolved CRITR spectra for two array diameters, with lineouts shown below the images indicating thermal (green) and non-thermal (blue) contributions to the Kα emission. Right: PCD traces for the two arrays along with comparisons of modeled and measured emission for the 70-mm diameter array.[10] The bottom plots show power and spectra as determined by the reduced analysis method described above. In parantheses, the inner/outer array diameter, array height, and total mass are given, and in the inset showing spectral data, the estimated yield in the Kα line is listed.

Based on this analysis, significant effort was devoted early in this LDRD to investigating smaller-diameter wire arrays, which were believed to produce more high-energy electrons than the larger arrays designed to maximize thermal temperatures. Changes to the load such as conical and twisted wire arrays and gaps in the cathode were all investigated (as described further below), but no single design change was found that would consistently increase the non-thermal K-shell yields from Mo or Ag wire arrays.

4 EXPERIMENTS TO IMPROVE Kα YIELD AND PULSE SHAPE

4.1 Mass and diameter optimization

To investigate trends in Kα emission, we have explored a large range of initial wire array setups. In previous work, data has shown similar changes to the wire array have had a large impact on the plasma conditions in the stagnated z pinch, and hence on the radiated output, including the thermal K-shell yield and pulse shape. Table 2 summarizes all of the shots performed related to non-thermal Kα emission. Note that, after scaling with photon energy was established within this dataset (e.g. see Figure 3), experiments concentrated on Mo sources as the Kα line is in a spectral range where the diagnostics on Z are more routinely fielded and hence present less risk to data return. The dynamics, and hence output, are expected to scale favorably to higher energy for each of these setups. Estimated yields of emission in the Ka line complex are given for the Mo arrays (in kJ).

Table 2: Non-thermal shots performed

Shot	*Material*	*Outer array Diameter*	*Outer array Diameter*	*Height (mm)*	*Mass mg (total)*	*Yield in Kα (kJ)*	*Aim/Notes*
2362	Mo	70	35	20	1.34	0.9	Scoping
2426	Mo	20	12	10	4.50	1.2	Scoping
2427	Mo	50	25	20	2.61	1.5	Scoping
2428	Mo	50		20	1.81	0.7	Single: Role of instabilities
2429	Mo	20	12	10	4.50	2.3	Recess: Vacuum gap
2430	Mo	50	25	20	3.48	1.1	Heavy: scoping
2533	Mo	50	25	20	2.68	0.6	Recess
2534	Ag alloy	50	25	20	2.61		Ag alloy: Material scaling
2535	Ag alloy	50	25	20	2.61		Recess
2654	Mo	20	12	10	4.50	0.8	Recess
2655	Ag pure	20	12	10	4.22		Scaling
2656	Ag alloy	20	12	10	3.92		Recess
2657	Mo	12-20	12	10	4.50	0.4	Conical
2658	Mo	12-20	12	10	4.50	0.4	Conical
2775	Mo	20	12	10	8.85	0.4	5 deg twist outer
2776	Mo	20	12	10	8.85	0.5	No twist, heavier than 2426
2777	Mo	20	12	10	8.85	0.4	45 deg twist outer
2823	Mo	20	12	10	8.85	0.4	45 deg twist inner
2842	Mo	70	35	20	2.74	0.6	Heavier than 2362
2843	W	70	35	20	2.75		Same mass as 2842

Experiments explored Mo wire array diameters of 20, 50 and 70 mm at various implosion times. Diameters were chosen both to provide a wide range of implosion velocities, but also to be similar to previous experiments on Z, thus allowing a broader data base of previous shots with which to compare (20 mm wire arrays were used for W wire arrays extensively on Z prior to the refurbishment and on a few shots since, 50 mm wire arrays have been used for Al implosions, and 70 mm wire arrays have been used for stainless steel implosions).

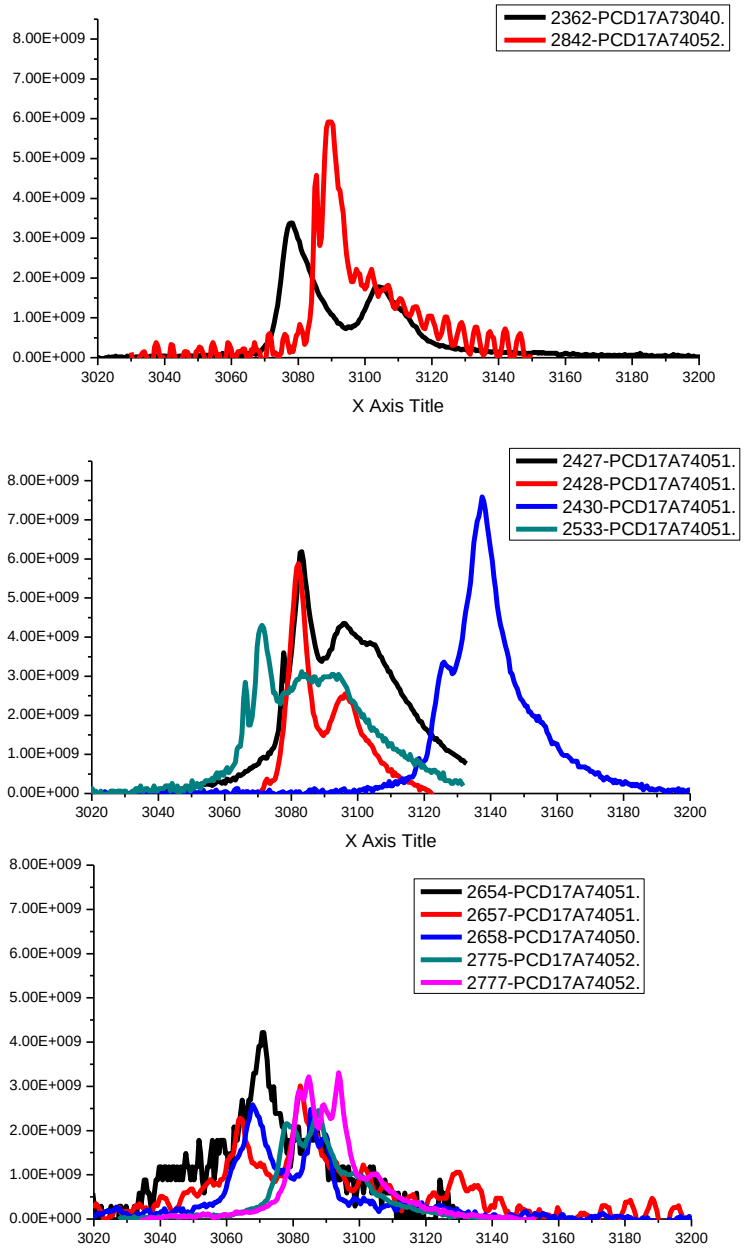

Figure 20: X-ray pulses dominated by non-thermal Kα emission for different Mo wire arrays. The majority of the traces are filtered with 28um Mo, with the exception of z2362, which is filtered with 20 um Titanium + 1500 um Kapton. The top plot shows two different masses at 70mm diameter, the middle plot shows two different array

masses at 50mm diameter, including repeat shots at one mass (black and olive) and a single wire array (red), and the bottom plot shows compact wire arrays.

Overall, the Kα output of the different configurations explored were all very similar, each radiating ~1-2 kJ at >15 keV, with about half of that output in the Kα line. The radiation pulse shape of the different setups do vary, with many of the radiation pulses shown above having multiple peaks and long tails. Towards the end of the LDRD project we attempted to improve the radiation pulse shape, which motivated performing the experiment with the larger diameter, heavy setup of z2842. This was motivated by simulations (Figure 21), which show tighter, more powerful soft x-ray pulses for the heavier masses at 70 mm, and was confirmed by the PCD data shown below. The two arrays had similar non-thermal Kα emission, but the heavier 70 mm array lacked much of the significant thermal component that had been observed in the lighter 70 mm array, and so had an overall lower yield. And although it imploded later than the lighter array, it also lacked a significant late-time emission peak, calling into question the inferences about the origin of non-thermal emission described in Section 3 above.

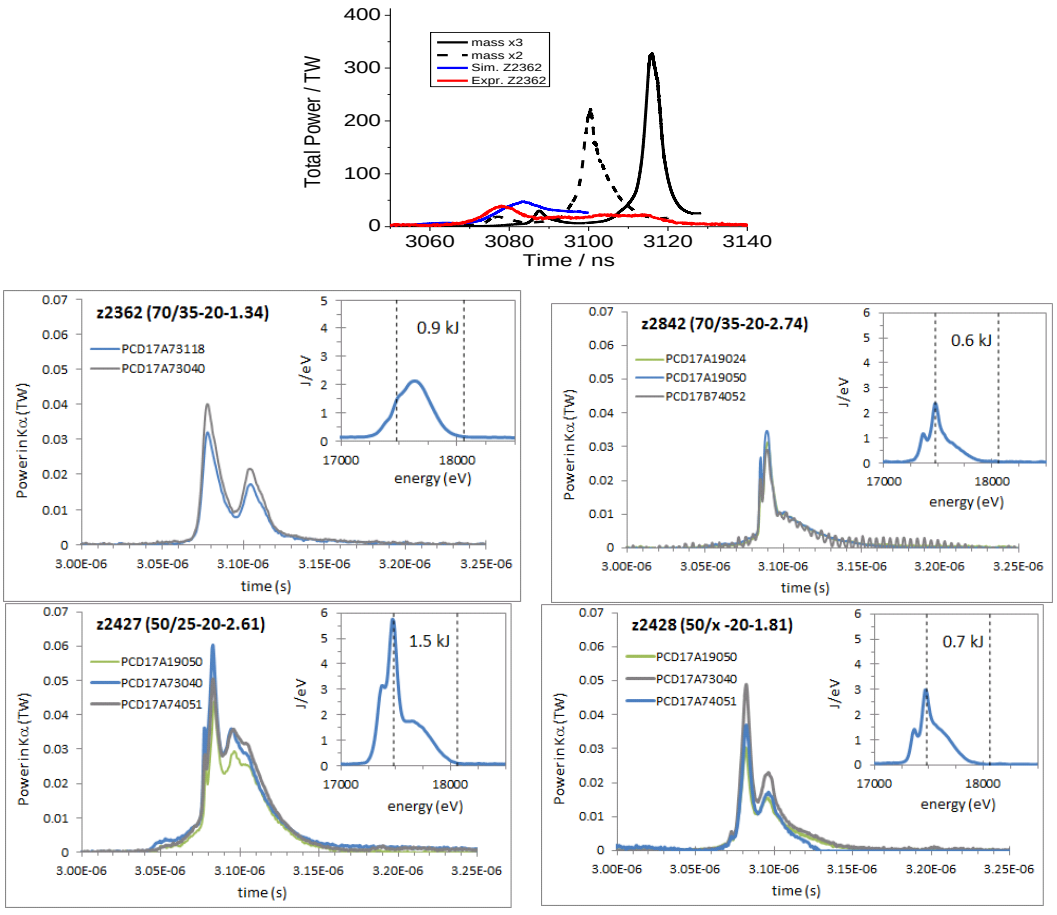

Figure 21: Top: Simulations of different mass of 70mm diameter implosions. Middle: Inferred Kα line powers and measured spectra from 70 mm arrays. Bottom: inferred Ka line powers and spectra from 50 mm arrays, including a single array.

4.2 Modifying plasma conditions along axis using conical wire arrays

Previous experiments[27] have demonstrated that conical wire arrays have the ability to produce axially varying plasma conditions on 1MA generators. Additionally they have the ability to create a vacuum gap at the base of the wire array due to the divergent angle to the current path. Both of these characteristics make these pinches interesting for non-thermal emission – the axially varying plasma conditions can be used to diagnose how the plasma conditions effect the emission, and the potential for a vacuum gap can lead to an enhanced beam (although in reality the electrons would be magnetized so are unlikely to cross the gap).

An axially resolved spectrum from a conical wire array is shown in

Figure 22. Kα lines are emitted from the full length of the z pinch, however are much brighter in the lower section of the image (the smaller diameter section of the conical array near the cathode). Additionally, near the cathode there is considerable emission at energies above the 17.4 keV cold Kα lines. As discussed earlier, this corresponds to Kα emission from L-shell ions, indicating that this section of the pinch is hotter than the top of the pinch. This is consistent with data in 27, where a considerable drop in temperature was observed from cathode to anode for an imploding conical wire array at 1MA peak current. However, the conical arrays did not have higher Kα yields than cylindrical arrays of similar mass and diameter.

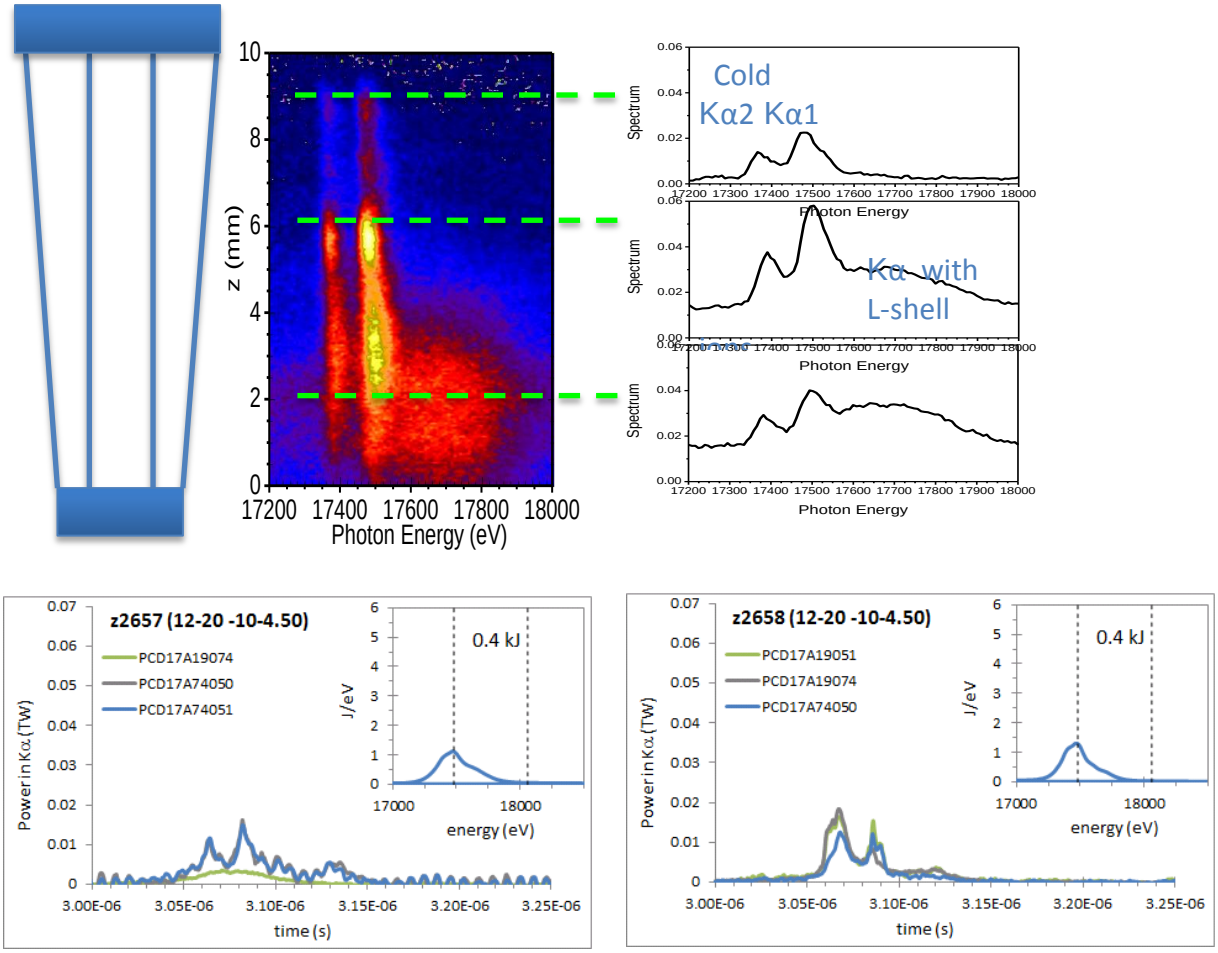

Figure 22: Top: Conical wire array setup, axially resolved spectrum and lineouts from the spectrum. Bottom: Ka power and spectra from two conical wire arrays.

4.3 Twisted wire arrays

We have performed experiments attempting to optimize both Kα yield and pulseshape. Some of these experiments have been empirical, and others have been guided by MHD simulations coupled to particle simulations (along with the physical insight which has arisen from those simulations).

In a z pinch there are large magnetic and electric fields. Electrons are highly magnetized and the electric field is attempting to accelerate them. For a typical z pinch implosion these two fields are perpendicular for the majority of the implosion. They can develop parallel components when the pinch disrupts and cylindrical symmetry is lost.

In an attempt to better harness the axial electrical field in a wire array z pinch, we performed experiments investigating the effect of twisting the wire array, as shown in Figure 23. The twist introduces an azimuthal current, and hence an axial magnetic field. Using this setup we were able to considerably improve the Kα power radiated by the pinch, however the yield radiated in the Kα line was not significantly changed, and although the Ka emission appeared to be dominated by non-thermal emission, with small contributions from thermal L-shell ions, overall the heavy 20 mm arrays did not perform as well as lighter and larger arrays

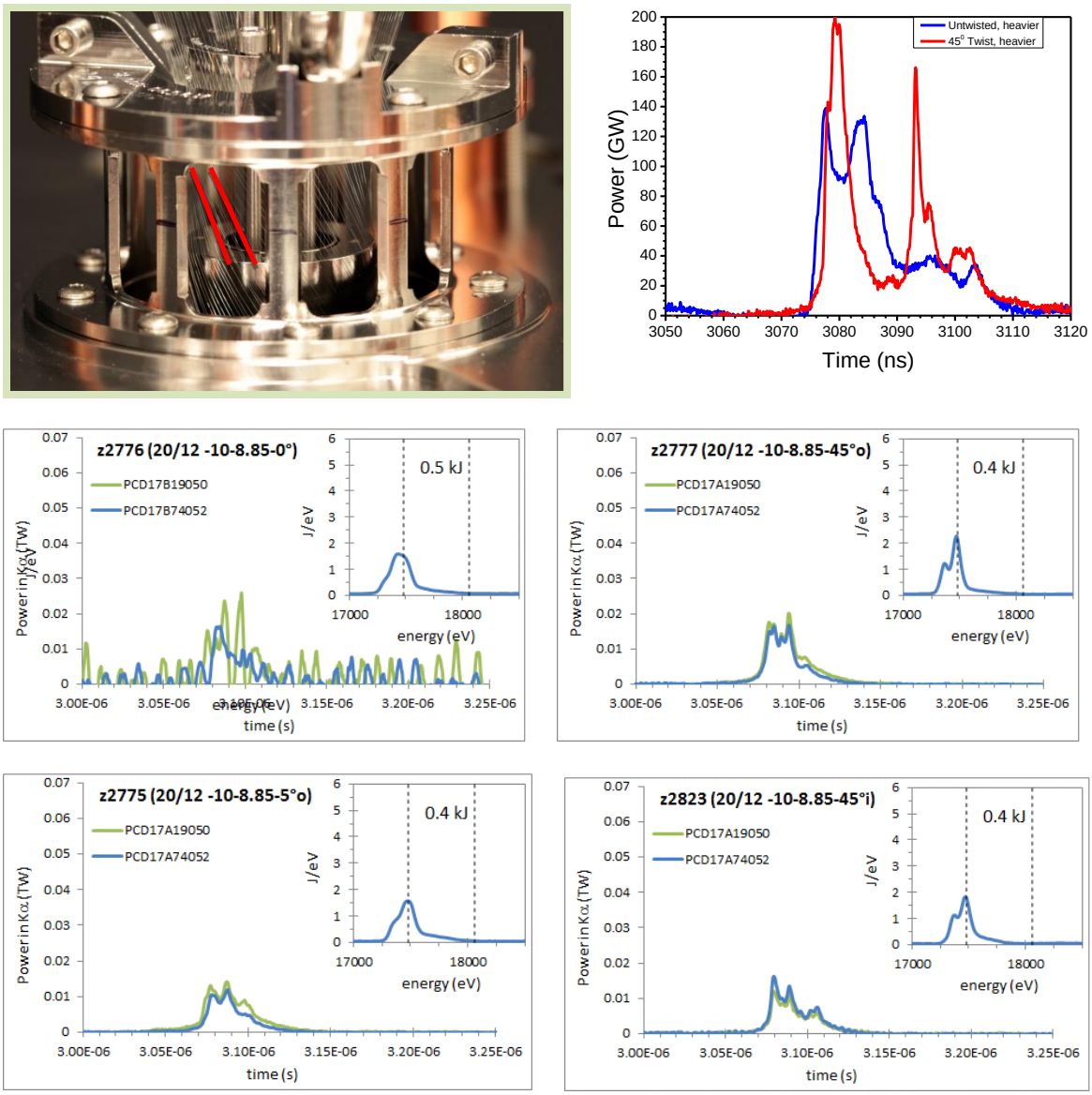

Figure 23: Top Left: Photo of a twisted wire array. Top Right: Radiation pulses from untwisted (blue) and twisted (red) wire array. The four plots below show Ka pulse shapes, spectral shapes, and yields from 8.85 mg arrays with various clocking of inner (i) and outer (o) arrays.

4.4 Using a recess in the cathode

Another attempt to enhance Ka yields was made by direct of a recess cut into the cathode at a diameter smaller than the inner wire array. There are a few possible mechanisms by which the recess could enhance the late-time Ka radiation. Firstly, as the imploding plasma passes the recess it could act as a plasma opening switch, quickly shunting the voltage out of the implosion producing a high voltage gap between the electrode and the plasma, and instead allowing that voltage to accelerate electrons into the plasma. Instead of creating a high voltage gap, the recess could also act to provide a region of low density plasma beneath the main pinch. In this region, there is likely to be a low magnitude highly non-uniform magnetic field from material washing around.

Figures 24b and c show the spectra and K-shell x-ray power for Mo experiments with and without the recess. From the data it appears the recess has significantly enhanced the energy radiated in the Kα line and significantly changed the K-shell pulse shape, with a sharp rise of this radiation late in the x-ray pulse. Note that the PCD detector used to record this power pulse saturated during the peak of the K-shell x-ray pulse, so the decay of the signal is not trusted, and this setup has only been used once on Z. Other PCDs also recorded anomalous late-time behavior on z2429, with a divergence in the Kα-scaled PCD traces indicating a significant enhancement of Ka line emission relative to the continuum level. Identical processing of the raw spectral data, too, indicated a significant enhancement of the Kα yield.

Unfortunately, attempts to repeat the high-yield experiment were unsuccessful, leading us to the conclusion that the apparent enhancement was an artefact either of the load or of the diagnostics. While similar setups recorded similar early-time Kα powers of ~0.02-0.04 TW, only the initial recess experiment (z2429) had significant late-time emission. Nonetheless, the experiments with a cathode recess were overall good performers with higher-than-average yields dominated by non-thermal Kα emission (albeit with rather large pulse widths).

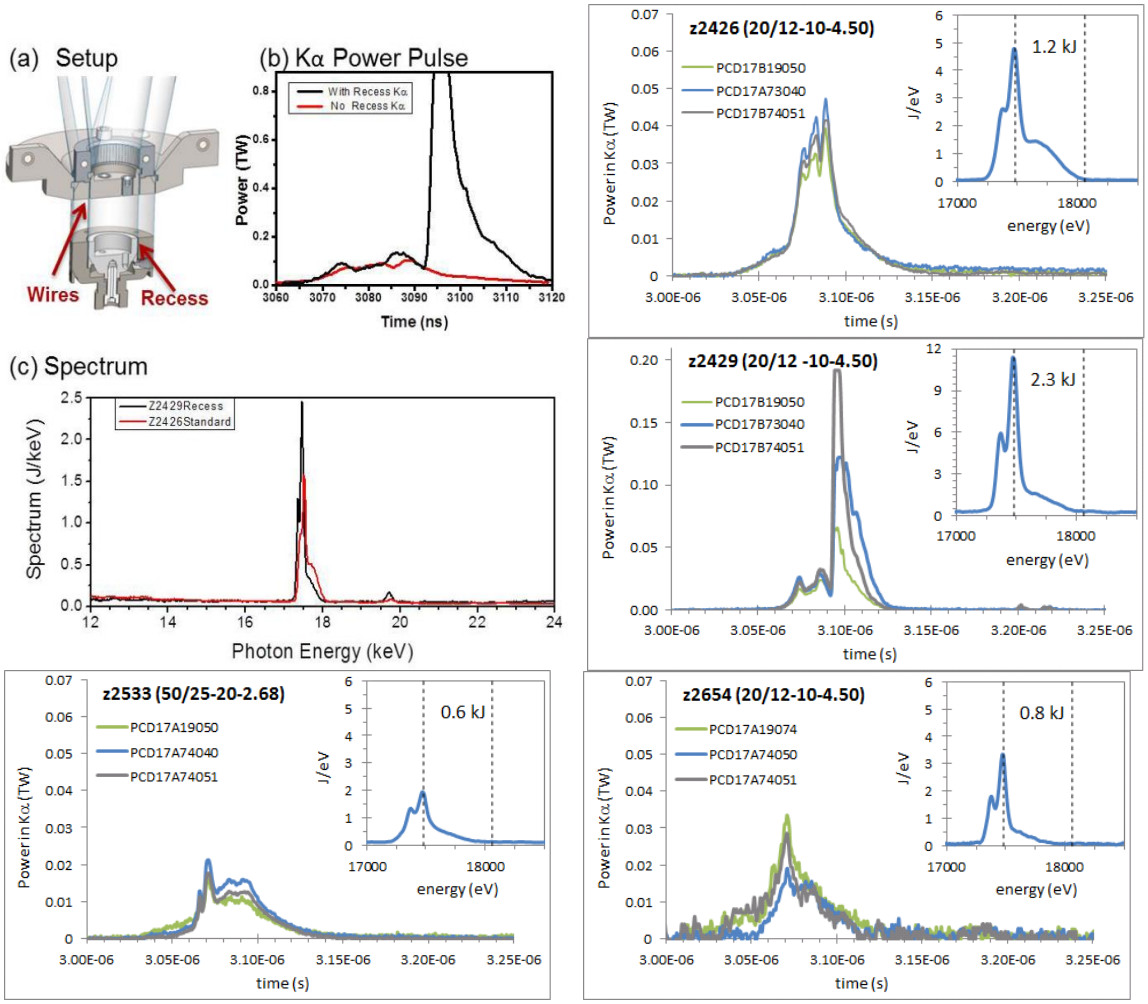

Figure 24: Top left: Setup for a compact Mo wire array with a recess in the cathode. (b) shows power pulse for this and an identical shot without recess (note that the black recess curve goes off-scale on the oscilloscope). (c) Spectra for the same comparison, processed in an identical way, apparently showing enhancement with the recess. *Note that this data could not be reproduced* Top right: Ka powers and spectra for arrays with and without recess. *:* Bottom: Kα powers and spectra from similar Mo wire arrays with a cathode recess.

5 INITIAL EXPERIMENT WITH W

In order to push the scaling trends shown in Figure 3 to higher photon energies, for one shot (z2843) a W wire array was used. Many of the recent diagnostic developments discussed in Section 2 of this report were leveraged in order to attempt a measurement on the W Ka line.

Two version of CRITR-X were fielded – one with axial resolution using a Quartz 203 crystal (aiming for Ka in second order) and one with radial resolution using a Quartz 502 crystal (giving Ka in first order). To increase the signal level for these instruments the intention was to field them without slits; unfortunately slits were fielded, reducing the efficiency of these instruments by approximately an order of magnitude. These instruments did not record data on this shot, however in the future they will again be fielded in this setup without the imaging slits aiming to record the Ka line.

TLDs were planned to be fielded, but due to Be contamination of some components prior to the shot this was not able to be fielded (the TLDs must be Be-free to be read – on the previous shot a filter had broken resulting in the complete inside of the instrument to be deemed Be contaminated until swipes are able to demonstrate it is clean).

The TIPC pinhole camera was fielded, and recorded data. Shown in Figure 25 is data from TIPC for both the W shot (z2843) and, as a null result, for the Mo shot (z2842) that immediately preceded the W shot, but using identical filters. The filter pair used in shown in the figure. The data indicates a significant difference in the exposure of the images associated with the different filters that do and don't transmit W Ka. For the null result there is a difference between the two images, but not a distinct as in z2843 (see the lineouts plotted in the figure). Analysis is ongoing on this data, and further shots will attempt to repeat this data point with a wider selection of diagnostics.

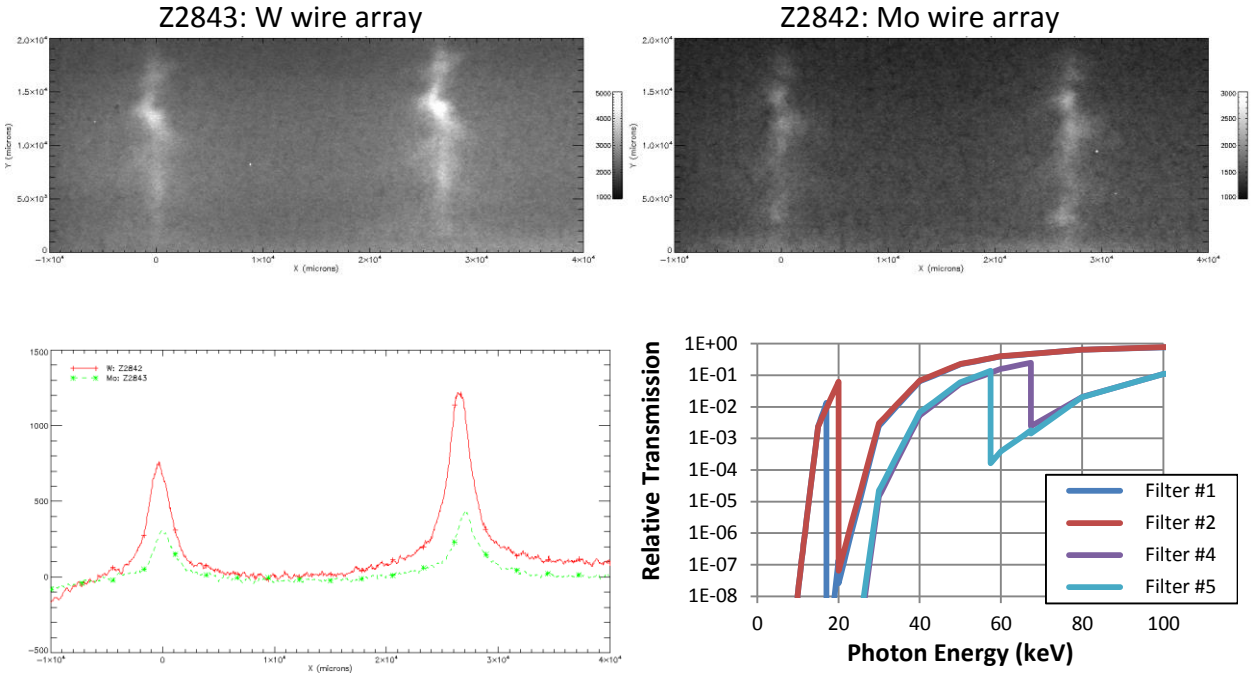

Figure 25: W and Mo pinhole images with a filter pair designed for W. Also shown are lineouts through the two pairs of images showing quantitative different in exposure. Finally shown are the filters used – the images and lineouts are from the pair in cyan (left of image pairs) and purple (right of image pairs).

6 Kα YIELD ESTIMATES FROM RUNAWAY ELECTRONS IN DENSE Z-PINCHES[28]

Wire-array z-pinch implosions on Sandia's Z facility produce ~kJ yields of Kα photons. We have developed a kinetic post-processing model which simulates the motion of accelerated electrons in the MHD electric and magnetic fields of the pinch, including their collisional interaction with the background plasma. We demonstrate that runaway electrons generated in the lower density outer regions of the stagnated pinch can eventually reach the inner dense regions, where they generate Kα photons. The yield from these runaway electrons is on the order of kJ, broadly matching that measured in experiments.

6.1 Overview

MHD simulations of these implosions fail to reproduce such high yields, most likely because they do not account for energetic electrons. In this report, we discuss some of the issues associated with modelling kinetic effects, give some arguments which form the basis of our first approach, and detail some of the results obtained by post-processing data from the GORGON MHD code with a collisional particle tracker.

There are many difficulties associated with the computational modelling of the Kα production process. Firstly, MHD models themselves are invalid in the lower density, high temperature regions, where the electrons are not collisional on timescales relevant to MHD evolution. Fortunately, due to the strong magnetization in these regions, the diffusive models of thermal transport are largely valid. It is also true that these lower density regions carry very little current and do not significantly affect the hydrodynamic evolution of the pinch, therefore the lack of validity of the MHD approximation there is usually of little concern. However, as we will consider in this paper, these regions may act as sources of runaway fast electrons which can contribute to or largely explain the total Kα yield.

Electron runaway occurs when the local electric force exceeds the collisional (frictional) force, usually stated in terms of the "Dreicer" electric field:

$$E > E_D = 5.8 \times 10^{-18} \ln \Lambda \frac{n_e}{T_e}$$

Which requires low density and/or high electron temperature. The electric field is usually taken from Ohm's Law combined with Ampere's Law:

$$\mathbf{E} = \frac{\eta}{\mu_0} \nabla \times \mathbf{B}$$

Note that other terms in Ohm's Law (for example the velocity-advection term or the Hall term), which are important for the pinch evolution via their effect on the magnetic field, do not contribute to electron runaway because they generate electric fields that are always

perpendicular to the magnetic field, and electron runaway cannot occur across a magnetic field (instead electrons undergo drift motion). By using the above expression for the electric field, we have avoided false contributions to the electric field caused by numerically evaluating the dot product between the true (total) electric field and the magnetic field:

$$E_{\parallel} = \frac{\mathbf{E}.\mathbf{B}}{B}$$

We justify focusing only on electrons in runaway regions by noting that in regions that are collisional, the electrons should not (on average) be able to gain significant energy from the fields and so their contribution to Kα production should not deviate significantly from the MHD predicted value. An important caveat is that electrons in the tail of the distribution, which non-locally transport heat from the lower density regions to the higher density regions, have not been included in our model (nor are they accounted for in MHD models). This simplification should be revisited in future.

Our research has been along two tracks: (i) Generating and tracking fast electrons as they accelerate around through the MHD background plasma in an effort to estimate total Kα yield. (ii) Performing fully-electromagnetic, kinetic simulations in one spatial dimension (but allowing 3D fields) to better understand how the MHD approximation breaks down in runaway regions. We will now discuss some of these results.

6.2 Particle Tracking Simulations

An example of the electric field produced by 3D GORGON simulations of a Z nested Molybdenum wire-array is shown in Figure 26 (density on the left, electric field on the right).

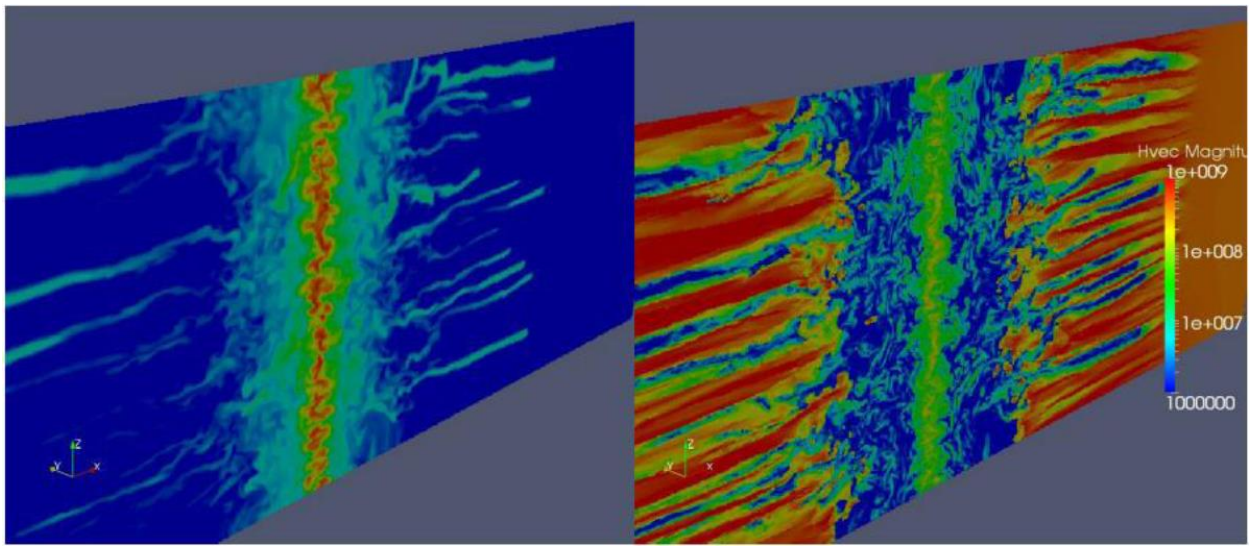

Figure 26: Density (left) and electric field from Gorgon for a nested Mo array on Z

The larger fields, of order Giga V/m, tend to exist in the lower density regions. A runaway condition is calculated for each computational cell using the (above mentioned) Dreicer field. Particle electrons are then generated in each runaway region (with a characteristic thermal+drift velocity) and propagated through the entire pinch for 1ns. We use a relativistic Boris pusher for acceleration and motion in the EM fields, with linear interpolation of the Gorgon fields to the particles. Each fast electron collides with both the background electrons and ions via a Monte-Carlo Fokker-Planck collision algorithm. We also accumulate the Kα yield on the grid by locally calculating the cross-section. Electrons with energy below the Kα threshold are ignored. This process is repeated, 8 times (i.e. we run with 8 particles per cell) for each cell in the entire computational domain (so long as the runaway condition is met, equating to about 33000 cells). The accuracy of this calculation requires that the MHD conditions do not vary substantially during the nanosecond time period. We resolve the electron gyro-orbits in the strong MHD magnetic fields, requiring very small computational timesteps relative to the ns integration period.

The total Kα yield is estimated in the following way: the yield in each cell is summed over the entire grid. This gives the total yield for all computational particles for one nanosecond. Next we relate the number of computational particles to the number of real electrons by assuming quasi-neutrality, which gives us an expression for the flux of electrons out of each cell. This flux can then be integrated over the 1ns time period to give us a multiplicative factor by which the yield must be increased to take account of the constant production of fast electrons during the nanosecond.

The final assumption is that the hot, dense pinch last for around 20ns, so that the total yield will be given by the previous integrated result (for 1ns) multiplied by 20. In other words, we have not yet run our code for 20ns, although this will be completed in the near future. Of course this gives order-of-magnitude estimates only, because we have assumed that the yield during one particular 1ns period (out of the 20ns of interest) is much like the yield during any other 1ns period. We have checked 3 arbitrary 1ns periods and indeed this seems to be the case. However, we are currently parallelizing the model to properly account for every 1ns period, to further refine our estimate. Yields of order ~5kJ are found in this manner, which is broadly in agreement with the experiments. It is also interesting to note that most of the Kα production occurs in the denser regions of the pinch, where some of the fast electrons deposit most of their energy. In Figure 27 is an example xy (r-theta) slice of the computational domain showing the relative Kα yield.

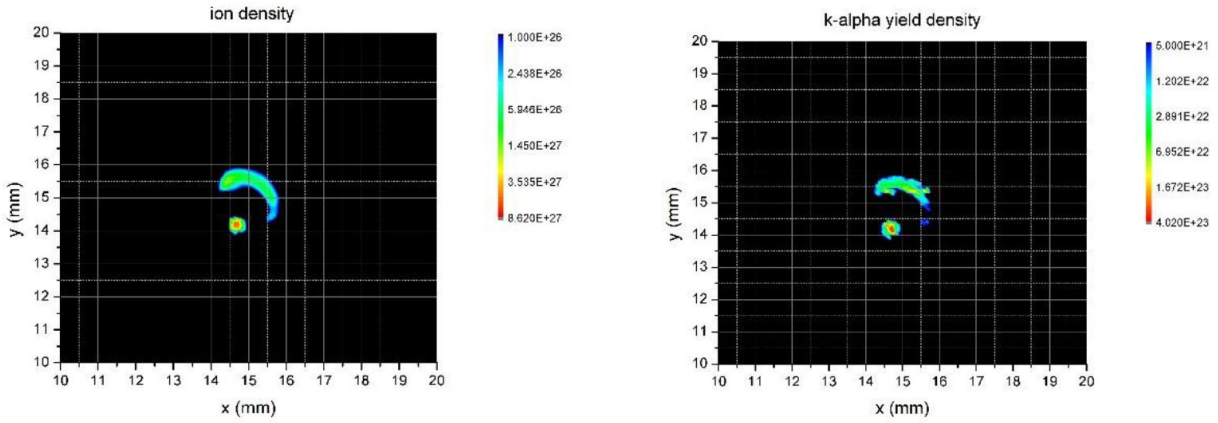

Figure 27: Kα emission from Gorgon. Density is shown on the left, Kα yield on the right. The correlation of Kα yield with background MHD density is clear.

It is not currently understood what causes a given fast electron to generate high Kα yields. We have attempted to search for correlations in our electron trajectories to identify important characteristics an electron must possess for it to significantly contribute to total yield. The strongest correlation is between the time-integrated background fluid number density that a fast electrons sees during its motion. This is not surprising – it simply means only electrons that reach the high density regions of the pinch have a large Kα cross section. The more relevant question is: how do some electrons eventually manage to reach the higher density regions? (Note that the runaway electrons are all generated in the lower density regions). Running total yield correlation diagnostics against the following variables has not yielded an obvious answer:

- Initial electron energy
- Final electron energy
- Initial radial position of the electron (there is some correlation here, related to the fact that electrons initialized at smaller radii find it easier to access the higher density regions which are also at smaller radii).
- Initial local magnetic field strength
- Initial electron magnetization parameter
- Initial local density and temperature

Only time-integrated data seem to give correlations, but these do not give us any useful hints on where to focus our computational effort, because there is no correlation with initial conditions. All that we know is that only electrons that are born within 4mm radius of the central axis make a significant contribution.

We will later explore the trajectories of the "top-ranked" Kα emitters in detail in an effort to understand how they escape magnetization and reach the core.

6.3 Electron tracking for 70-mm & 20-mm diameter Mo arrays on Z

With some appreciation of the plasma conditions that are favorable to electron runaway (locally co-aligned electric and magnetic fields), we may explore how variations in the experimental load configuration can potentially enhance this process. Or at least better understand where and when during a wire arrays evolution conditions favorable to electron acceleration develop. We follow the techniques developed by J.Chittenden B, Appelbee and M.Sherlock, and previously presented at DZP 2014 and described above. We describe in more detail two cases representative of the range of experiments fielded on Z. A 20mm diameter compact Mo nested wire array imploded early in the Z current pulse, and a 70mm diameter, low wire number nested Mo wire array.

Wire array evolution is loosely divided into three stages; ablation, implosion and stagnation. Early in the current pulse low density material is ablated from stationary, dense wire cores. When wire mass is depleted to the point where wires begin to break through the array begins to implode, accreting the precursor plasma ablated into the array interior. MRT instabilities seeded during ablation rapidly grow and disrupt the imploding shell, leaving some fraction of the mass trailing behind the main implosion. A second wire array nested within the first partially resets instabilities, allowing better convergence of material on axis. As array material stagnates on axis kinetic energy is rapidly thermalized forming a hot dense plasma, however residual kinetic energy, and the continued action of the drive current rapidly disrupt this plasma column.

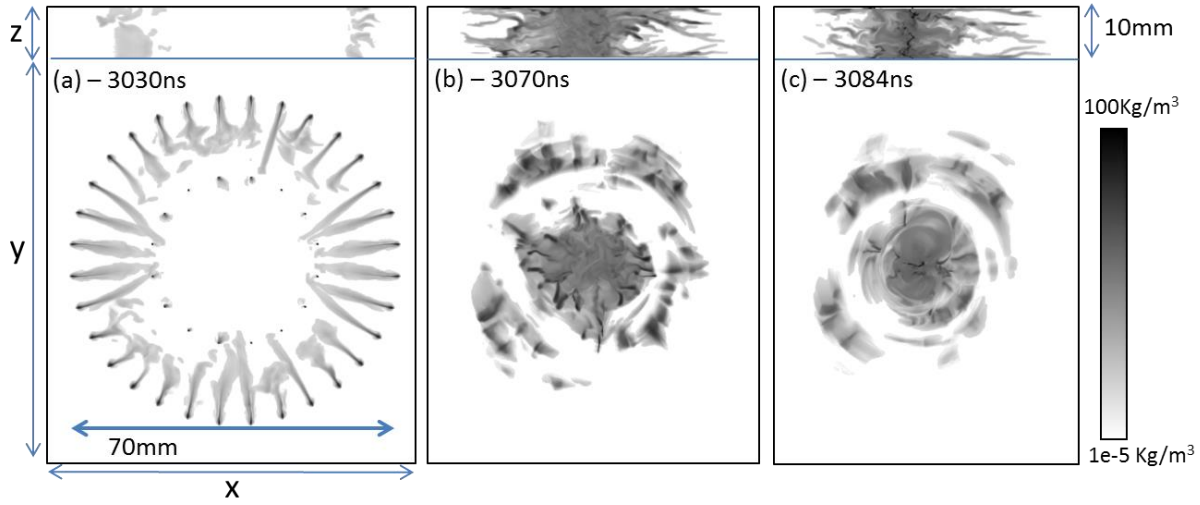

Figure 28: Axial (top) and radial (bottom) slices through a simulation of a 70mm diameter Mo wire array on Z.

These stages of array evolution are illustrated in Figure 28 for a 70mm, low wire number nested wire array consisting of 30 on 15 13.6 micron diameter Molybdenum wires fielded as Z shot 2362. While these loads were 20mm tall, only 10mm of the height is modelled here. The very low wire number is primarily dictated by the low array mass needed to implode from large radius, and the lack of availability of finer Mo wires. It is known that increasing wire number

typically increases pinch uniformity, however for the purpose of electron acceleration a high degree of uniformity is not necessarily desirable. Figure 29 shows comparison of the simulated and total soft x-ray power radiated by this array, with the very broad total x-ray pulse widths resulting from the high degree of disruption.

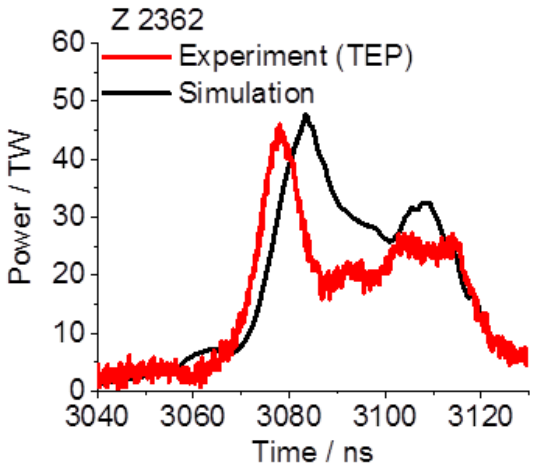

Figure 29: Comparison of simulated total power to experimental power.

During ablation (Figure 28(a)) the large initial inter-wire gaps allows the local magnetic field around each wire to more aggressively drive m=0 instabilities in the wire (typically stabilized by ablation flow in higher wire number implosions). This exacerbates early time disruption of the array and leads to particularly aggressive instability growth in this configuration. While disruption from instabilities is typically undesirable for most wire array radiation sources, for electron driven Kα sources some degree of instability growth may be necessary to promote regions of electron acceleration. As the array implodes low density highly structured mass is left trailing behind the imploding front (Figure 28(b)). Current flow is redirected around some of this structure creating regions where a local component of the electric field can become partially aligned with the magnetic field. Such partial field alignment in low density plasma creates regions where the Dricer criteria for acceleration of electrons is exceeded and electrons may be liberated. These regions are highlighted in red in Figure 30 during the early stages of stagnation on axis (at approximately peak soft x-ray emission).

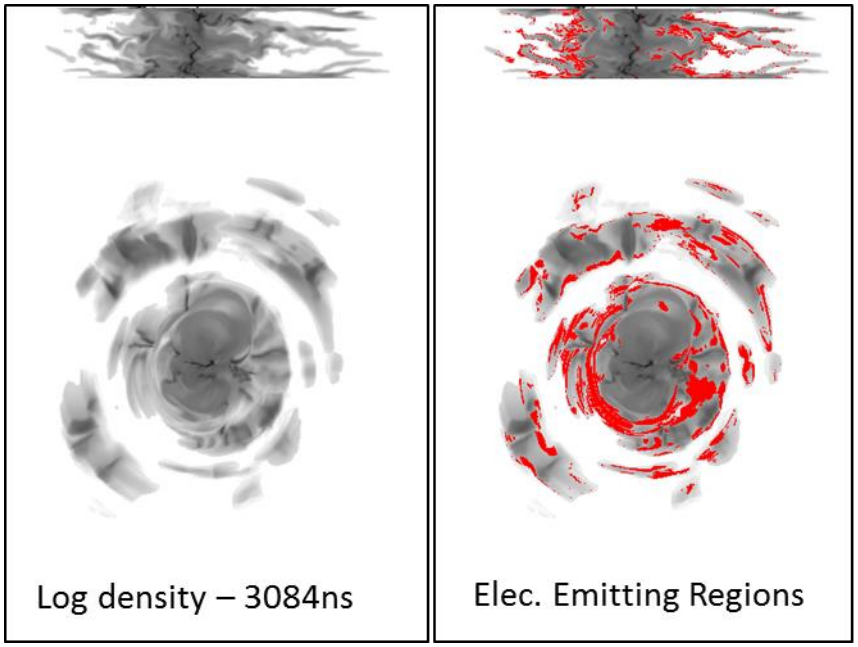

Figure 30: Side-on (top) and end-on (bottom) log density plot and log density overlaid with electron emitting regions

At this time a large volume of plasma at large radius is able to liberate electrons, but as previously noted it is unclear how effectively these electrons can migrate to regions of higher plasma density formed on axis during stagnation. Since the electrons are highly magnetized they cannot easily cross azimuthal field lines to accelerate into smaller radii.

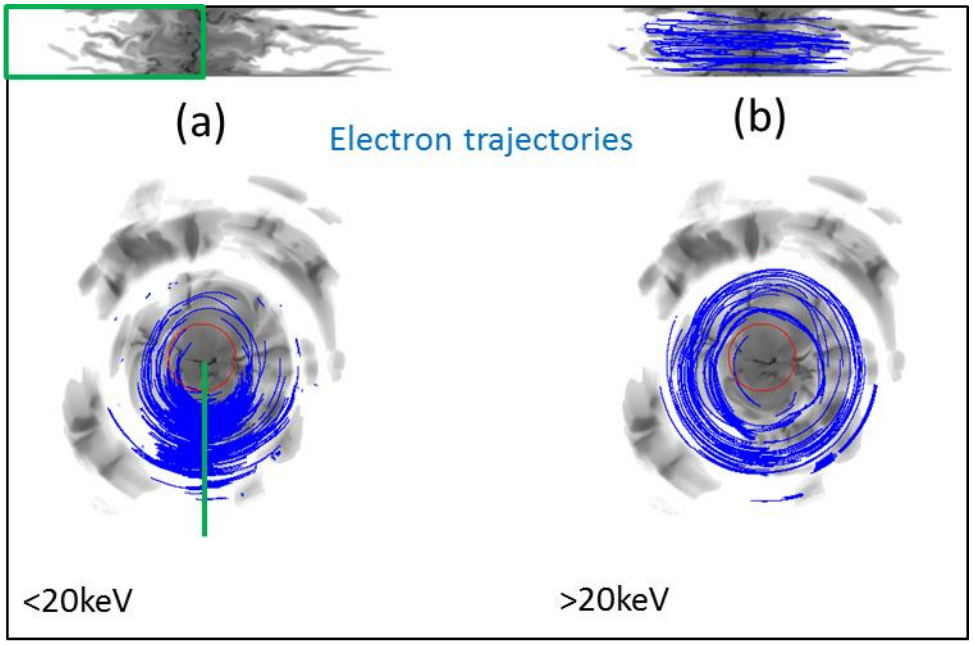

Figure 31: Electron trajectories for <20 keV electrons and >20 keV electrons. Electrons are sourced on the green surface shown on (a).

Figure 31 shows projections of the trajectories from electrons emitted from the r-z plane indicated by the green line, and the green box in Figure 31(a). Electrons shown are only those emitted from outside a radius of 5mm (red circle shown). Electron trajectories are divided into two classes representing those accelerated to above and below 20keV energies. The electrons that are not accelerated to energies higher than ~20keV (Figure 31(a)) remain in the general vicinity of the plane from which they were emitted. A small fraction (~4%) of the emitted electrons are successfully accelerated to energies where they may start to contribute to Mo k-shell emission, however as shown in Figure 31(b), these electrons are trapped on magnetic field lines circling the plasma, unable to migrate into small radius. Plasma densities in the trailing mass at large radii are low, and since the cross section for k-shell ionization is small (~70 barns) the contribution to Kα emission from this region is likely to be relatively small. Looking instead at the central region below a radius of 5mm (inside the red circle in Figure 31), the unstable nature of the stagnating column results in small regions where co-alignment of electric and magnetic fields is sufficient to promote electron acceleration. At this time these regions constitute less than 2% of the electron emitting volume, however given the higher plasma densities in the vicinity of the axis they provide ~15% of the total number of electrons accelerated. Furthermore, given higher current densities at small radius, a larger fraction (12%) of these electrons are able to achieve energies exceeding 20keV. For this array configuration the number of higher energy electrons provided by the central stagnation volume can therefore be comparable to those more easily accelerated from the lower density trailing mass (within a factor of 2).

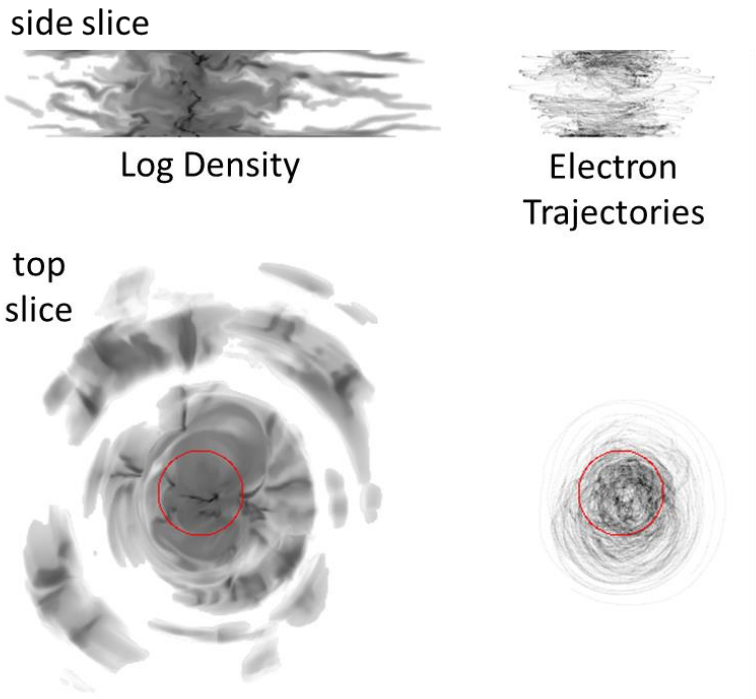

Figure 32: Density and trajectories shown side—on and end-on to the pinch.

Electrons liberated from the central volume follow trajectories enabling them to range more freely over the denser regions of the stagnated plasma (Figure 32), so it is primarily these electrons that are likely to contribute to Kα emission. The distribution of Kα emission reconstructed form this calculation is shown in Figure 33 indicating it is primarily associated with the dense stagnating plasma around the axis. We show emission integrated up to the time indicated, where Figure 33 also shows the logarithmic density distribution at this time. Regions from which electrons may be accelerated (those where the electric field exceeds the Dricer criteria) are indicated in red as before.

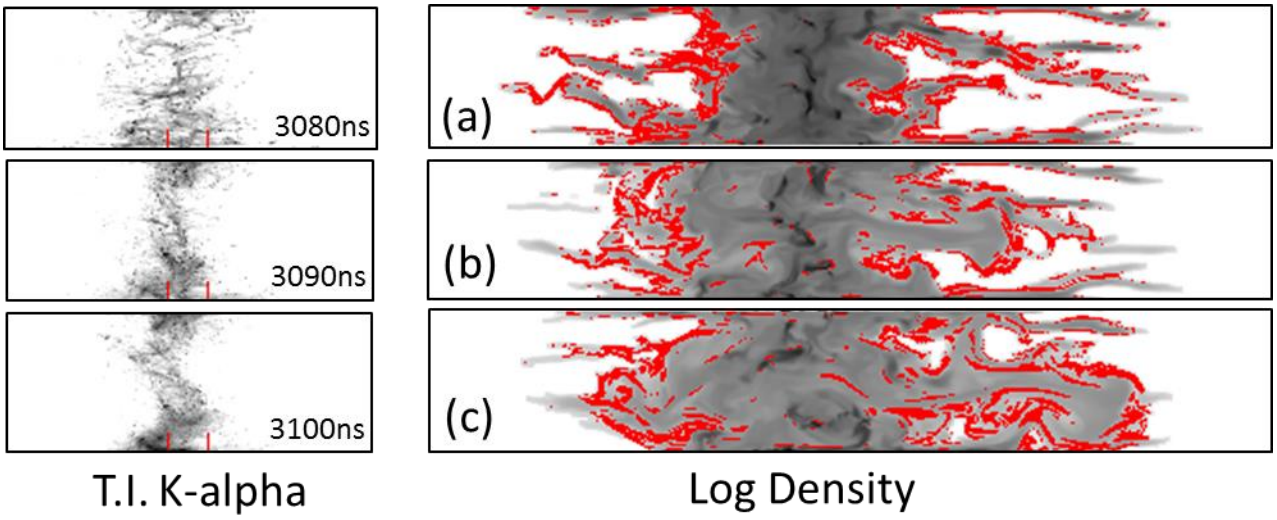

Figure 33: Kα emission and density. Red indicates the regions where the Dricer criteria is met.

The three times shown start at peak soft x-ray power and cover the disassembly of the stagnated plasma (x-ray power pulses shown in Figure 34. Since electrons liberated at large radius are unable to interact with dense plasma on axis, we rely on electrons born in close proximity to stagnation column. Whereas for the trailing mass we could rely on contorted current flow around highly structured plasma to create regions of field alignment, for the stagnation column we must wait for it to disrupt and disassemble before these conditions arise. Figure 34 compares the Kα x-ray power pulse to the total soft x-ray power pulse. Since the technique we employ cannot accurately assess the absolute number of electrons initially accelerated, the Kα power pulse is in arbitrary units.

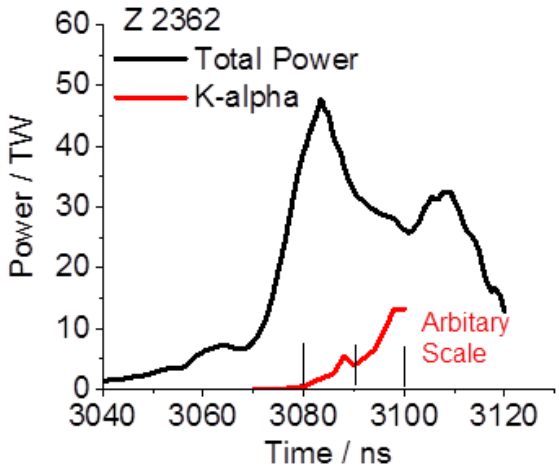

Figure 34: Simulated Kα and total power pulses for a 70 mm diameter Mo array.

At peak soft x-ray power, Kα production is negligible, as are the number of red electron acceleration regions adjacent to the stagnation column (Figure 33(a)). As the pinch disassembles, regions of electron acceleration develop on the surface of dense lumps of the fragmenting column (Figure 34 – 3080ns). It is these regions that are contributing the electrons useful to Kα production. The Kα power pulse is seen to rise later in time than soft x-ray production and is associated with fragmentation and disassembly of the pinch (Figure 33(c)).

Essentially the same evolution is seen in the 20mm diameter arrays imploded. Figure 35 compares soft x-ray power with the Kα power pulse (again on an arbitrary scale) for a 50 on 28 wire nested array consisting of 26.73 micron diameter Mo wires. Again we see Kα emission peaks in the tail of the soft x-ray power pulse (Figure 35(a)).

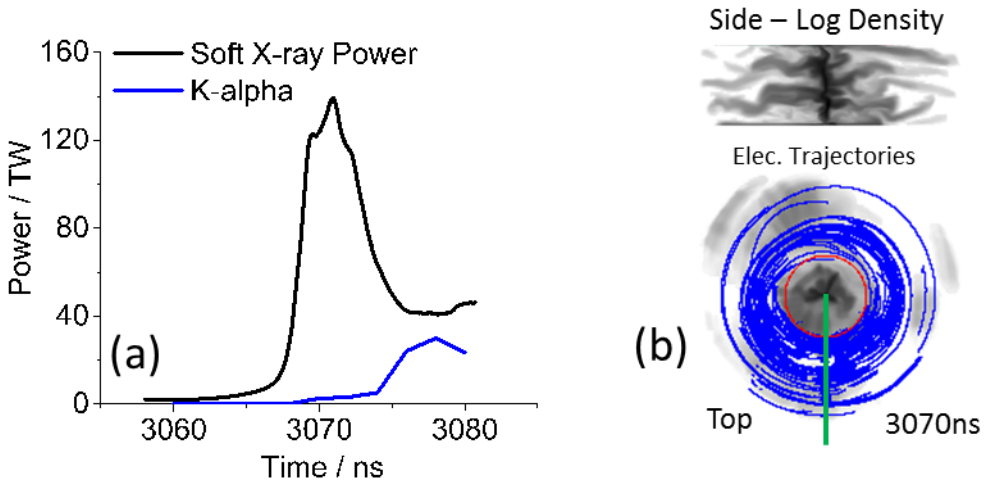

Figure 35: 20mm nested array (a) soft x-ray power and Kα power pulse. (b) Electron trajectories overlaying log density profile at time of peak soft x-ray power.

At peak soft x-ray power electrons liberated from the low density trailing mass (outside the red circle in Figure 35(b)) are unable to migrate in to interact with the dense column of stagnating plasma. Comparing the electron emission regions (red regions in Figure 36) as stagnation proceeds, a large volume of low density trailing mass is able to emit electrons, but electrons emission from regions adjacent to the dense stagnating column do not arise until post stagnation fragmentation of the pinch.

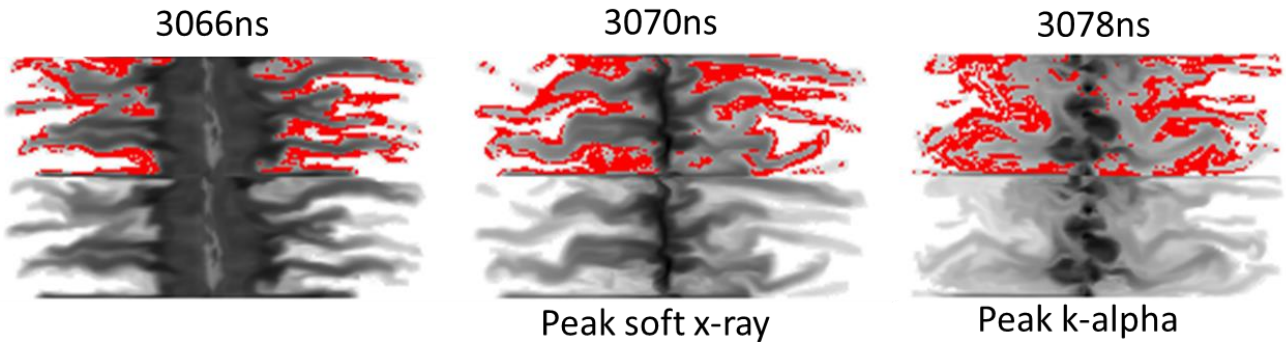

Figure 36: Distribution of electron emitting regions in side on cross sections plotting over logarithmic density profiles during stagnation and disassembly of the pinch on axis.

While qualitatively the behavior of the 70mm and 20mm arrays is the same, quantitatively assessing changes in the level of k-alpha emission is difficult with this method. We identify plasma regions and times where conditions are conducive to emission. Although without more self-consistent treatment of the charge depletion created by acceleration of some fraction of the electrons in the plasma, we cannot quantitatively assess the number of electrons accelerated. Neither can we determine how electron trajectories are affected by local buildup of charge, which may be significant in allowing (or further precluding) migration of electrons into denser regions of plasma.

6.4 Fully EM Kinetic Simulations of the Runaway Process

The above calculations rely on MHD data which inherently assumes Ohm's Law to be correct in order to determine the electric field. However, since runaway only occurs in regions that are not collisional (by definition), the validity of Ohm's Law should be questioned.

In order to understand this, we have developed a 1D fully electromagnetic PIC model. Only 1D is computationally feasible, due to the need to study vastly different time- and length- scales (i.e. both displacement current timescales and collisional timescales, and both EM wavelengths and pinch spatial scales). The model includes the full time-dependent set of Maxwell's equations and electron inertia, and we have successfully benchmarked it against Ampere's Law for a resistive wire carrying a current, also reproducing the skin-effect, the Ohmic electric field and the correct diffusive magnetic field in the plasma and in the vacuum.

The standard setup is that of a dense plasma in the center of the computational grid surrounded by vacuum. An external electric field is applied perpendicularly to the spatial axis of the simulation (representing the generator EMF), which drives a current through the plasma. This current induces an electric field in response to the external field, which also gives rise to EM waves that propagate out into the vacuum and eventually settle down to give the magnetic field predicted by Ampere's Law. When we allow the edges of the plasma to gradually fall to a low density (as in the case of a stagnated pinch), they become partially collisionless and satisfy the runaway criteria.

Figure 37 shows the 1D electron density and magnetic field (Bz) which is generated after equilibrium is reached.

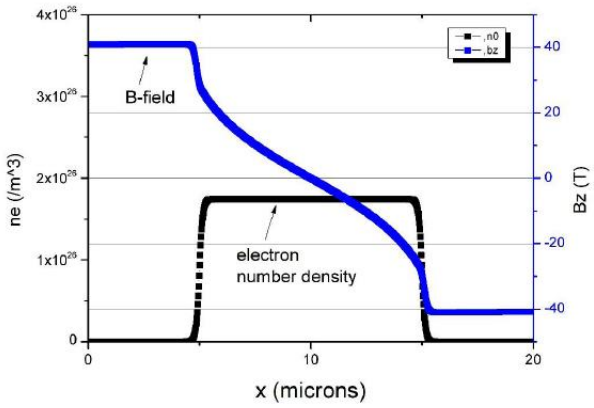

Figure 37: 1D electron density and magnetic field (Bz) which is generated after equilibrium is reached

The electric field (Ey) corresponding to this simulation is shown below (along with the Ohm's Law predicted electric field) in Figure 38.

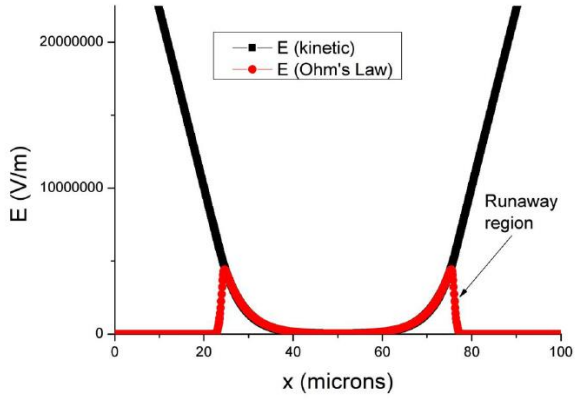

Figure 38 Electric field and Ohms law

As mentioned, the edges of the plasma are undergoing electron runaway – one of these regions is indicated on the RHS (there is also a corresponding runaway region on the LHS). The Ohm's Law prediction correctly matches the kinetic electric field inside the dense region of the plasma,

but fails to correctly match the field in the runaway regions. The real field is higher than the Ohmic field because the temperature rises at the edge due to the runaway process, which in turn lowers the resistivity and therefore lowers the Ohmic electric field. The kinetic simulation requires that the electric field be smooth near the edge, otherwise EM waves are generated until a smooth equilibrium is reached. Since the electric field in the vacuum must be finite in order to provide the correct Poynting flux into the plasma, the kinetic simulations preserve a smooth transition from this vacuum field to the dense plasma field.

Note that the above simulations do not necessarily mean the field solver in GORGON will fail to reproduce the correct field, since GORGON's field solver separates the vacuum and plasma solutions for the field, and will most likely join the two smoothly. Therefore, it may be possible to obtain a reasonable estimate for the field in runaway regions if they neighbor vacuum regions. Understanding how the kinetic simulations compare to the GORGON solution is a topic of current research.

Future improvements to our model should probably focus on the self-consistent generation of electric field (ignoring as a first step the self-consistent modifications to the magnetic field, which is dominated by the dense pinch evolution). For example, it would be instructive and relatively straightforward to initialize all higher-temperature regions with PIC particles and fix the magnetic field (to the MHD value) but allow the electrons to generate a self-consistent electric field, which should act to simply confine them, while allowing for non-local heat transport to take place in a manner that conserves energy. The reason why electrons from non-runaway regions cannot be studied with the current computational model is that we do not use a self-consistent electric field, but instead rely on the MHD-generated electric field, which, not surprisingly, does not guarantee the total particle energy is conserved.

7 CONCLUSIONS

Experiments have been performed exploring non-thermal Kα emission on the Z generator. Such sources use less energy for ionization, and hence are expected to provide a flatter scaling to higher photon energy (i.e. with increasing Z). Data confirms favorable scaling of this type of x-ray source to photon energies >20 keV . Significant diagnostic development was needed to push measurement capabilities beyond 25 keV. Following this, an initial attempt was made to measure the 59 keV W Kα line to better constrain scaling. While, for various reasons, this shot had limited data return it will be repeated in December 2015.

The details of Kα emission were studied extensively using Mo wire arrays (where diagnosis is less risky than higher Z materials). Data indicated that the array setup (i.e. mass and diameter) have a significant effect on the radiation pulse, with some cases providing muli-peaked x-ray pulses with long tails, but other cases providing a clean single x-ray pulse. Twisting the wire array, which is expected to provide an axial magnetic field component within the pinch, was also found to be advantageous to the radiation pulse shape.

Significant progress has been made in simulating Kα emission in wire array z pinches. Prior to the present work, no effort had been put into this problem, partially because of the need to model both the dense plasmas (which require an MHD code) and the electrons which require tracking as particles. Through collaboration with Imperial College these implosions have been modeled using a number of post-processing and hybrid techniques. Simulations have aided in experiment design and are likely to be necessary to further our understanding on Kα emission from Z pinches and how to optimize it.

As well as the LDRD project described here, this work has engaged a number of collaborators to start investigating Ka emission from wire array z pinches. The Naval Research Lab has begun collaborating with University of Nevada Reno and Cornell University to study Kα emission on 1MA generators, particularly with the aim of gaining benchmark data to mature Kα simulation capabilities at NRL.

Going forward, the radiation effects program at Z is planning to continue this work. Short term, there are experiments planned for December 2015 aimed at further improving the radiation pulse shape from the pinch, again attempting a measurement on the W Kα line and to assess the effectiveness of a solid rod as a Kα radiator within the pinch. During 2016 there are plans to continue data analysis and modeling to determine the best path forward for any future shots.

Finally we note that a vast amount of data has been collected as part of this project. The present state of analysis of representative data has been presented here, however data processing and analysis is ongoing, and final interpretations will be presented in more detail in the peer-reviewed literature.

REFERENCES

1. C.A. Coverdale et al., High Energy Density Physics 6, 143 (2010)
2. D.J. Ampleford et al., Physics of Plasmas 21, 056708 (2014)
3. M.E. Cuneo et al. Phys. Plasmas 13, 056318 (2006)
4. M.C. Jones et al.. Review of Scientific Instruments 85, 083501 (2014)
5. H.-S. Park, et al., Review of Scientific Instruments 75, 4048 (2004)
6. P. D. Lepell, et al., Physics of Plasmas 12, 032701 (2005); A. Dasgupta, et al., High Energy Density Physics 9, 347 (2013); S. B. Hansen et al., Physics of Plasmas 21, 031202 (2014)
7. C. Deeney, et al., AIP Conference Series, 195, 55 (1989); I. Shrestha, et al., IEEE Transactions on Plasma Science 38, 658 (2010).
8. D.J. Ampleford et al., Physics of Plasmas 20, 103116 (2013)
9. C.A. Jennings et al., Physics of Plasmas 22, 056316 (2015)
10. S.B. Hansen et al., Physics of Plasmas 21, 031202 (2014)
11. D.J. Ampleford et al., IEEE International Conference on Plasma Science, Washington DC, 2014
12. R. B. Spielman, Rev. Sci. Instrum. 66, 867 (1995).
13. T. Nash, M. Derzon, R. Leeper, D. Jobe, M. Hurst, J. Seamen, Rev. Sci. Instrum. 70, 302 (1999).
14. D.B. Sinars et al., Rev. Sci. Instrum. 82, 063113 (2011).
15. D.J. Ampleford et al., Physics of Plasmas 21, 031201 (2014)
16. Y.Cauchoism Journal de Physique, 3, 320 (1932).
17. L. T. Hudson, et al. Rev. Sci. Instr. 73, 2270 (2002).
18. J.Seely, et al., J. Quant. Spect. Rad. Trans. 81, 421 (2003); J.Seely, et. al. J. Quant. Spect. Rad. Trans. 99, 572 (2006); J.Seely, et al., Appl. Opt. 47, 2767 (2008).
19. G. Loisel, J. Seely. in preparation
20. M. Sanchez del Rio, et al., J. Appl. Cryst. 48, 477 (2015).

21. Meadowcroft, A. L., Bentley, C. D., & Stott, E. N.. Rev. Sci. Instr., 79, 3102, (2008)

22. C. I. Szabo, U. Feldman, S. Seltzer et. al., Opt. Lett. 36, 8 (2011)

23. L.A. McPherson et al., in preparation

24. T. J. Webb. “Theoretical design and experimentation of an autoacceleration system for the Idaho State Induction Accelerator System (ISIS).” Ph.D. dissertation, Idaho State University, June 2007.

25. M.J. Berger, J.S. Coursey, M.A. Zucker and J. Chang. “Stopping-Power and Range Tables for Electrons, Protons, and Helium Ions.” NIST online database. Updated August 2005. http://www.nist.gov/pml/data/star/index.cfm

26. T. J. Webb. “High-impedance coaxial autoacclerator.” IEEE Trans. Nucl. Sci., Vol. 54, No. 6, Dec. 2007.

27. D.J. Ampleford et al., Physics of Plasmas, 14, 102704 (2007)

28. M. Sherlock, J.P. Chittenden et al., in preparation

DISTRIBUTION

1 Imperial College London (electronic copy)
Attn: Jeremy Chittenden
Blackett Laboratory
Prince Consort Road,
London SW7 2BW
United Kingdom

1 Naval Research Laboratory (electronic copy)
Attn: John Giuliani
4555 Overlook Avenue SW
Washington, DC 20375-5346

1	MS1106	David Ampleford	1683 (electronic copy)
1	MS1106	Christopher Jennings	1684 (electronic copy)
1	MS1106	Guillaume Loisel	1683 (electronic copy)
1	MS1178	Timothy Webb	1656 (electronic copy)
1	MS1186	Stephanie Hansen	1684 (electronic copy)
1	MS1193	Daniel Sinars	1680 (electronic copy)
1	MS1196	Gregory Rochau	1683 (electronic copy)
1	MS0899	Technical Library	9536 (electronic copy)
1	MS0359	D. Chavez, LDRD Office	1911 (electronic copy)


Sandia National Laboratories